



An Enhanced Deep-Learning Catalog of the Mw 8.8 Maule Aftershock Sequence

Rodrigo Flores-Allende¹, Léonard Seydoux¹, Éric Beaucé^{2,3}, Luis Fabian Bonilla^{3,1},
Philippe Gueguen⁴ and Claudio Satriano¹

¹Université Paris Cité, Institut de physique du globe de Paris, UMR 7154, Paris, France

²Lamont-Doherty Earth Observatory, Columbia University, New York, NY, USA

³Université Gustave Eiffel, Champs-sur-Marne, Marne-la-Vallée, France

⁴ISTerre, Université Grenoble Alpes/CNRS/Univ. Savoie Mont-Blanc/IRD/Université Gustave Eiffel,
38000 Grenoble, France

Corresponding author: floresallende@ipgp.fr

Peer-review status:

This manuscript has been submitted for publication in JGR: Solid Earth and is currently under its first peer review. Future versions may contain different content.

An Enhanced Deep-Learning Catalog of the M_w 8.8 Maule Aftershock Sequence

Rodrigo Flores-Allende¹, Léonard Seydoux¹, Éric Beaucé²,
Luis Fabian Bonilla^{3,1}, Philippe Gueguen⁴ and Claudio Satriano¹

¹Université Paris Cité, Institut de physique du globe de Paris, UMR 7154, Paris, France

²Lamont-Doherty Earth Observatory, Columbia University, New York, NY, USA

³Université Gustave Eiffel, Champs-sur-Marne, Marne-la-Vallée, France

⁴ISTerre, Université Grenoble Alpes/CNRS/Univ. Savoie Mont-Blanc/IRD/Université Gustave Eiffel,
38000 Grenoble, France

Key Points:

- Improved catalog of the M_w 8.8 Maule earthquake aftershock sequence over 10 months.
- Deep-learning workflow for detection, location, relocation, and magnitude estimation.
- Increase of ca. 12 times the number of detections compared to previous catalogs.
- Highlight new statistical insights and tectonic structures.

Corresponding author: Rodrigo Flores-Allende, floresallende@ipgp.fr

Abstract

We re-examine the aftershock sequence of the M_w 8.8 Maule earthquake in south-central Chile using deep-learning on 10 months of continuous seismic data from 156 temporary stations along the rupture zone (March 2010–March 2011). By integrating back-projection and matched filtering with PhaseNet (a deep-learning phase picker), we initially identify 99,137 earthquakes. We then relocate these events using NonLinLoc with source-specific station terms and waveform coherence. We select a subset of 8,894 earthquakes for template matching and obtain a final catalog of 374,058 earthquakes—nearly 12 times more than previous studies—achieving a magnitude of completeness of M_w 1.7, which is an order of magnitude better. The spatiotemporal evolution of the seismicity reveals intricate seismic structures, including a highly active shallow cluster in the Pichilemu-Vichuquén region (33.5°S–35°S) showing a complex L-shaped geometry and deeper slab-related seismicity near Concepción (37°S–38°S). Spatial and temporal variation of the b -value further highlight heterogeneous post-seismic deformation driven by multiple fault system activations. This study demonstrates how modern analytical techniques, particularly machine learning, extract valuable insights from older datasets, enabling the discovery of previously undetected small-amplitude seismicity and refining our understanding of earthquake dynamics and seismic hazards.

Plain Language Summary

After a large earthquake, understanding how the Earth’s crust adjusts is crucial for improving seismic hazard assessments. Seismologists study these processes using earthquake catalogs, which document the timing, location, and magnitude of recorded events. Both large and small earthquakes provide valuable insights into the physical processes at play within the crust, as their relative distribution reflects underlying stress and deformation mechanisms. However, the quality of catalogs depends on how well earthquakes can be detected, located, and measured. Small-magnitude events, in particular, are more challenging to identify due to background noise and variations in data quality. This study enhances the aftershock catalog of the 2010 M_w 8.8 Maule earthquake in south-central Chile by analyzing 10 months of continuous seismic data from 156 temporary stations. By applying modern techniques, including artificial intelligence and machine learning, we identify over 375,000 earthquakes—nearly 12 times more than previous catalogs. The expanded catalog provides a significantly more detailed view of aftershock distribution, revealing complex seismic patterns. It highlights shallow activity primarily associated with crustal faults and deeper seismicity linked to the subducting slab. We also examine the b -value, which quantifies the ratio of large to small earthquakes. Variations in the b -value offer key insights into how stress evolves over space and time, suggesting a combination of processes driving post-seismic deformation. Our study demonstrates how modern computational techniques can extract valuable information from historical seismic datasets. By constructing more detailed earthquake catalogs, these methods improve our understanding of seismicity and contribute to better earthquake hazard assessments.

1 Introduction

On February 27, 2010, a M_w 8.8 earthquake struck the Maule region in central-south Chile, causing significant loss of life and widespread damage (Salazar & McNutt, 2011). The rupture extended 500 km along the convergence margin between the Pacific and Nazca plates, between latitudes 33°S and 38.5°S (Figure 1a). This event ranks among the largest instrumentally recorded earthquakes worldwide, and is the strongest well-recorded in Chile (e.g., Delouis et al., 2010; Madariaga et al., 2010; Moreno et al., 2010; Vigny et al., 2011; S. Ruiz et al., 2012; Hicks et al., 2014; S. Ruiz & Madariaga, 2018). Its rupture coincides with the mature seismic gap left by the M_w 8.3 earthquake of 1835 (see e.g., Campos et al., 2002), and overlaps segments of previous major earthquakes, including the M_w 7.7 Talca (1928), M_w 8.1 Concepción (1960, e.g., Ojeda et al., 2020), and M_w 7.8 Arauco (1975) earthquakes.

66 It also partially overlaps the M_w 9.5 Valdivia earthquake area of 1960, the largest earthquake
 67 ever recorded in history (e.g., Madariaga et al., 2010; S. Ruiz et al., 2012).

68 Large megathrust earthquakes, such as those related to subduction zones, are typically
 69 followed by an increase in seismic activity known as aftershocks. Earthquakes are considered
 70 aftershocks when their magnitude is at least one unit smaller than the mainshock (Báth,
 71 1965), and can persist for weeks to years (Bilek & Lay, 2018). They result from stress per-
 72 turbations induced by the main rupture (Felzer et al., 2004), and their distribution across
 73 the rupture zone often correlates with regions of high post-seismic strain and substantial
 74 static stress changes (Lange et al., 2012; Rietbrock et al., 2012). Among the many after-
 75 shocks of the Maule earthquake, shortly after the mainshock, two large aftershocks of M_w
 76 6.9 and M_w 6.7 struck the area of Pichilemu on March 11, 2010, at the northern edge of the
 77 rupture zone (Fariás et al., 2011; Lange et al., 2012; Rietbrock et al., 2012; Ryder et al.,
 78 2012; J. A. Ruiz et al., 2014). These aftershocks suggest a potential migration of seismicity
 79 or the reactivation of analogous fault systems in the region.

80 A clear understanding of aftershock patterns, afterslip distribution, and triggering
 81 mechanisms is key to improving our knowledge of earthquake mechanics (Peng &
 82 Zhao, 2009; Yao et al., 2017; Minetto et al., 2022). For instance, S. Ruiz et al. (2017)
 83 used repeaters to reveal aseismic processes before and after the 2017 M_w 6.9 Valparaiso
 84 earthquake, suggesting that small-scale seismicity may have triggered the mainshock and
 85 played an important role in the rupture dynamics. However, current studies mainly rely on
 86 large-magnitude aftershocks, as detecting smaller ones remains challenging. Seismic noise
 87 often hinders the detection of low-magnitude aftershocks, particularly when using traditional
 88 methods based on signal amplitude such as Short-Time-Average over Long-Time-Average
 89 trigger (STA/LTA, see e.g., Allen, 1982). Other factors, such as wave scattering and at-
 90 tenuation, further complicate the detection of small aftershocks, especially in regions with
 91 extensive rupture zones and sparse seismic networks like in the present study (Figure 1b).

92 Recent advances in deep learning have significantly improved the quality of earthquake
 93 catalogs (Ross et al., 2019; Mousavi & Beroza, 2023; Zhu & Beroza, 2019). These methods
 94 excel at identifying low-magnitude events and provide more reliable locations, unveiling the
 95 intricate details of seismic sequences and fault structures (Beaucé et al., 2019; Tan et al.,
 96 2021; Beaucé et al., 2022; Mancini et al., 2022; Minetto et al., 2022). In this study, we use
 97 these techniques to reassess an old, but distinctive dataset recorded by the International
 98 Maule Aftershock Deployment (IMAD, see e.g., Beck et al., 2014), a mobile seismic net-
 99 work that was deployed within weeks after the Maule earthquake, covering the rupture zone
 100 from north to south (Figure 1a). We present a high-resolution earthquake catalog of the
 101 Maule aftershock sequence and a spatiotemporal analysis of the seismicity. Our aim is to
 102 uncover previously unresolved features related to the rupture dynamics during the after-
 103 shock sequence of the Maule earthquake over a 10 month period. The strategy is based on
 104 Beaucé et al. (2024), a deep-neural-network automatic seismic phase picking (Zhu & Beroza,
 105 2019) associated in space with backprojection (Frank & Shapiro, 2014) to detect and locate
 106 earthquakes and two relocation stages (Lomax, 2001; Lomax & Savvaidis, 2022) to build
 107 an initial catalog. Subsequently, we apply a template matching with the detected events
 108 (Gibbons & Ringdal, 2006; Frank & Shapiro, 2014; Beaucé et al., 2018) to identify new
 109 earthquakes, which may otherwise be missed by conventional techniques, thus increasing
 110 the catalog resolution (Minetto et al., 2022).

111 In the following sections, we first outline the tectonic context of central-south Chile,
 112 with a focus on the 2010 Maule earthquake and its aftershock sequence. We then introduce
 113 the IMAD database and the BeamPower and Matched-Filtering (BPMF, Beaucé et al.,
 114 2024) method used for earthquake detection and location, applying this approach to nearly
 115 10 months of seismic data covering the entire rupture zone. Next, we detect, locate, and
 116 relocate events based on the quality of automatic picks, estimate moment magnitudes, and
 117 perform a Gutenberg-Richter analysis, including new methods for calculating the b -value.

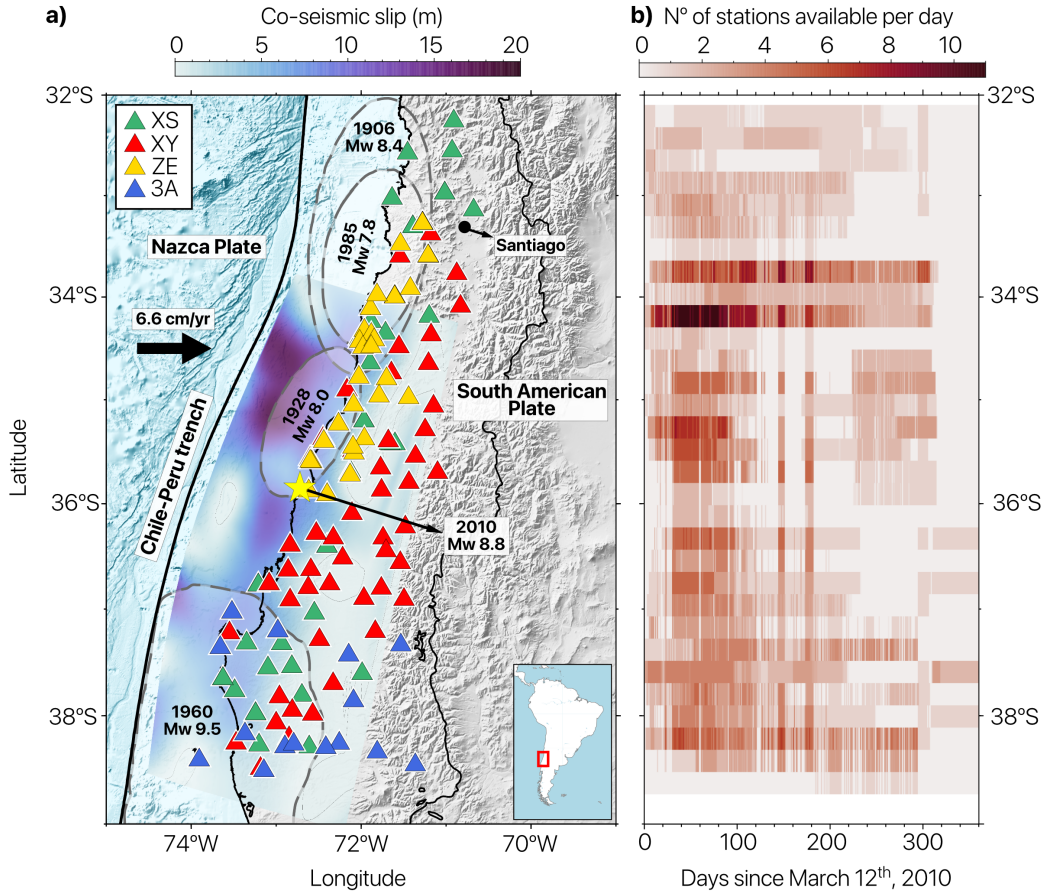


Figure 1. Study area and data coverage. (a) Seismic stations deployed in south-central Chile after the mainshock (triangles). Each color represents a network managed by different institutions: RESIF (XS in green, Vilotte & et al., 2011), University of Florida (XY in red Steve Roecker & Ray Russo, 2010), GFZ (ZE in yellow), and University of Liverpool (3A in blue, Beck et al., 2014). The coseismic slip model presented by (Yue et al., 2014) is represented in background colors, with darker zones related to larger slip. The yellow star marks the location of the mainshock on February 27, 2010. Historical rupture areas are depicted with gray ellipses. (b) Spatiotemporal availability of data. The color indicates the daily density of stations available every 0.2° of latitude.

118 Finally, we analyze the spatiotemporal distribution of seismicity in the catalog and compare
 119 it with previous catalogs to assess improvements in catalog resolution.

120 2 Data and Methods

121 We retrieve one year of seismic data from the International Maule Aftershock De-
 122 ployment (IMAD), a post-seismic mobile network operated by France, the United States,
 123 Germany, the United Kingdom, and collaborating partners, covering from March 2010 to
 124 March 2011 (see e.g., Beck et al., 2014). This seismic array included nearly 156 instru-
 125 ments equipped with accelerometers, short-period seismometers, and broadband seismome-
 126 ters (Figure 1a). Stations were deployed across the entire rupture area (Figure 1a), though
 127 not all operated simultaneously or for the same durations (Figure 1b). Also, external con-
 128 ditions caused fluctuations in station availability over time, making the dataset less stable

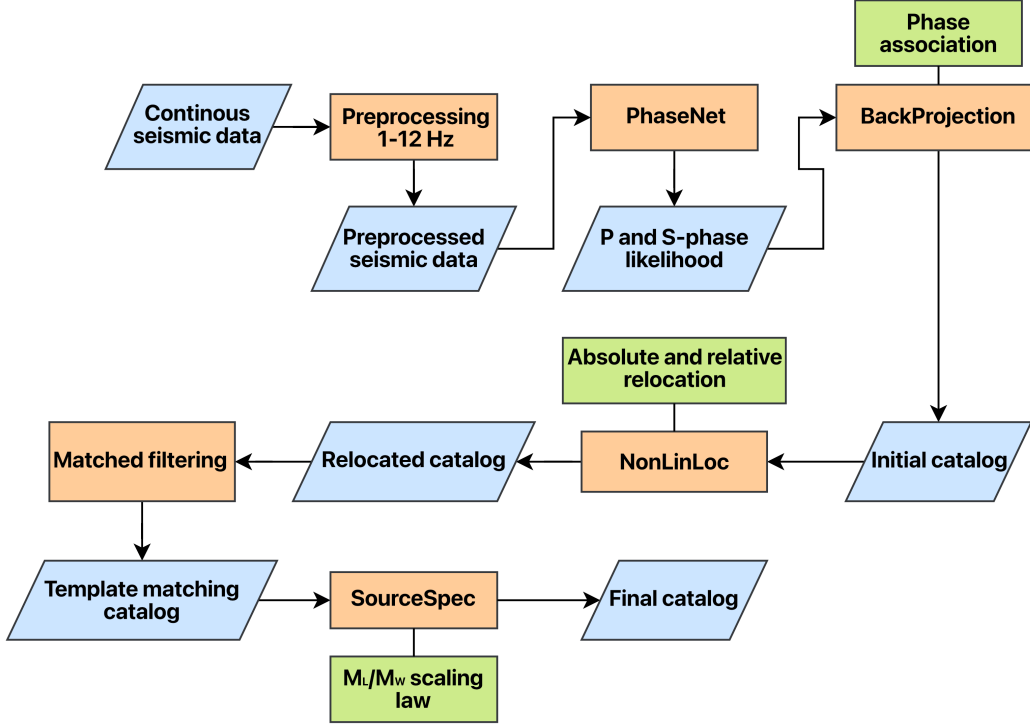


Figure 2. Earthquake catalog workflow. Blue boxes represent data (inputs or outputs), orange boxes indicate operations, and green boxes highlight some key steps. Continuous seismic data are filtered between 1 and 12 Hz and processed with PhaseNet to identify *P* and *S*-phase likelihoods. We associate the phases in space with backprojection to detect and locate the initial events, and relocate them with NonLinLoc. Additional techniques, such as template matching, contribute to increase the catalog completeness, while SourceSpec enables the magnitude estimation.

129 and uniform (Lange et al., 2012), so that at certain periods, fewer than 20 stations were
 130 operational, while at maximum, nearly 120 stations were simultaneously active.

131 To mitigate this variability, we exclude stations and traces with substantial data gaps.
 132 In regions with multiple stations within a 500 m radius, we select one station to avoid redun-
 133 dancy. Finally, we focus on periods with consistent availability of at least five stations,
 134 defined as the lowest threshold providing sufficient spatial and temporal coverage. The
 135 sequential steps of the workflow are illustrated in Figure 2, with further details provided
 136 in the subsequent sections. This workflow is based on the BPMF algorithm (Beaucé et
 137 al., 2024) which outputs are post-processed with NonLinLoc-SSST-Coherence (Lomax &
 138 Savvaidis, 2022) to enhance earthquake locations, and SourceSpec to estimate the moment
 139 magnitudes (Satriano, 2021). These tools complement the original framework, and were
 140 included to increase the robustness of the results.

141 2.1 Seismogram preparation

142 We first bandpass-filter the continuous data within 1 and 12 Hz to discard low-frequency
 143 noise. We select this frequency range from a visual inspection of data, which show energy
 144 concentrations mainly above 1 Hz. This approach is consistent with the parameters applied
 145 by Cabrera et al. (2021) in a similar tectonic context. Furthermore, we resample the data to
 146 a sampling rate of 25 Hz to reduce computational costs without compromising the efficiency

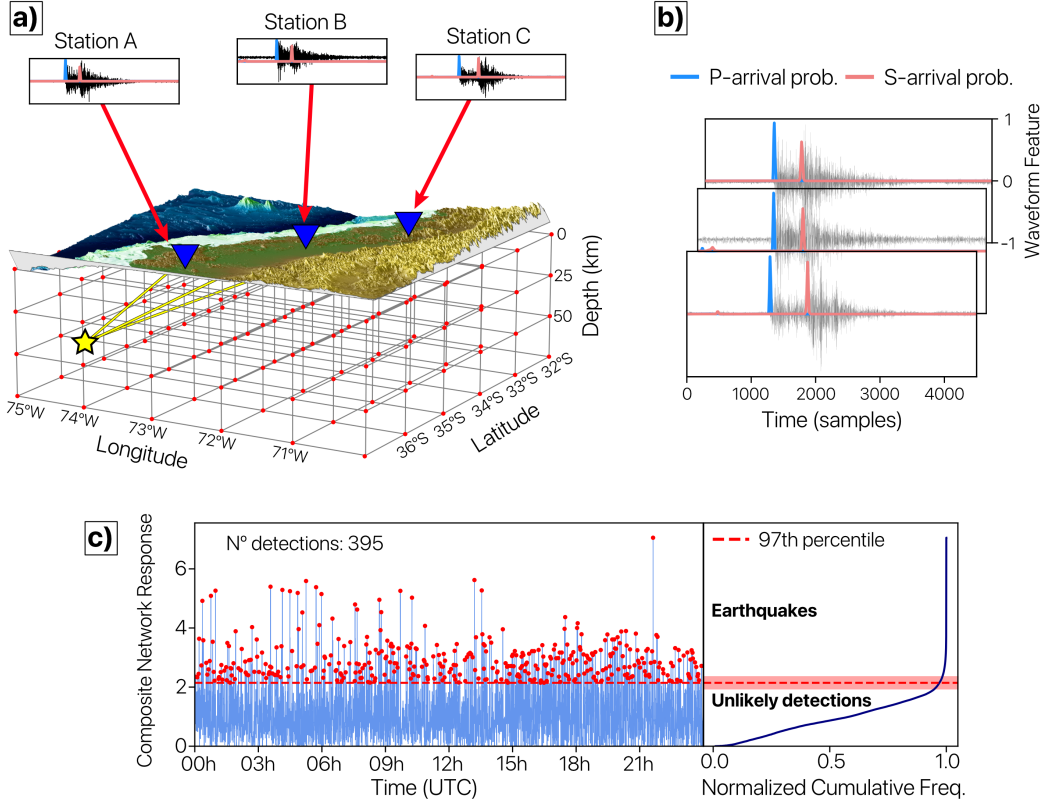


Figure 3. Earthquake detection and initial location. (a) Illustration of the grid with tested source points. The yellow star indicates the true earthquake location, with corresponding signals recorded at the seismic stations. (b) Example seismic record with the P and S likelihoods obtained using PhaseNet (Zhu & Beroza, 2019, respectively in blue and orange). (c) Composite network response obtained by shifting and stacking the waveform features for each component and station over time (Beaucé et al., 2024). The detection threshold is indicated with a dashed red line, with red points indicating events interpreted as localized sources.

147 of our analysis. In addition, we ensure the inclusion of only stations with minimal data gaps
 148 and consistent operational records. We include data segments if they met two key criteria:
 149 (1) a minimum total duration of 75% of the expected recording period for the event or
 150 station, ensuring sufficient temporal coverage despite potential gaps, and (2) individual
 151 contiguous chunks with a duration of at least 600 s, excluding excessively short fragments
 152 unsuitable for the analysis.

153 2.2 Initial earthquake detection and location

154 To detect and locate the initial earthquakes, we build a 3D spatial grid of potential
 155 point sources (Figure 3a). We calculate the travel time of P and S waves for each tested
 156 source withing a 1D velocity model for South-Central Chile (Hicks et al., 2014) adapted to
 157 include the slab geometry from the Slab 2.0 model (Hayes, 2018), as presented in Figure S1
 158 from the Supporting Information. We also apply a Gaussian smoothing filter to minimize
 159 abrupt velocity changes between layers, reducing artifacts in earthquake locations. This
 160 approach accounts for finite-frequency effects and prevents the formation of guided waves
 161 at sharp velocity discontinuities.

162 We compute the travel times (or moveouts) τ_{sk}^ϕ from each point source k to every station
 163 s for the seismic phase $\phi \in \{P, S\}$ by solving the eikonal equation (White et al., 2020). We
 164 use the deep learning automatic phase picking algorithm PhaseNet (Zhu & Beroza, 2019)
 165 to estimate the probabilities $\nu_{s\phi}(t)$ of P - and S -wave arrivals in continuous seismic data
 166 (as illustrated in Figures 3b, and S2). Next, we delay $\nu_{s\phi}(t)$ according to the computed
 167 moveouts and stack the waveform features to identify the most likely source location. This
 168 serves as an efficient seismic phase association mechanism (see also Figure 3b). The stacked
 169 response, also named beamforming by Frank and Shapiro (2014), is defined as:

$$b_k(t) = \sum_{s \in \mathcal{S}_k} \sum_{\phi \in \{P, S\}} \nu_{s\phi}(t + \tau_{sk}^\phi). \quad (1)$$

170 Coherent seismic signals produce higher values of $b_k(t)$ when aligned with a likely source k ,
 171 whereas incoherent noise does not contribute constructively. The set of seismic stations \mathcal{S}_k
 172 only considers the ten closest stations to the source k to enhance source-to-station sensitivity.
 173 The final source location is determined by identifying the maximum value of the composite
 174 network response (CNR) defined as the beamforming maximum over time $\mathcal{B}(t) = \max_k b_k(t)$.

175 The CNR allows the detection and location of earthquakes with increased sensitivity
 176 and precision (Beaucé et al., 2019, 2022, 2024). It provides an initial estimate of the event
 177 location by identifying the time at which the beam power reaches its peak. However, the
 178 accuracy of this location strongly depends on the grid resolution and the velocity model.
 179 A finer grid, with more potential source points k , improves spatial precision but drastically
 180 increases computational cost. A key challenge in this process is to distinguish between beams
 181 corresponding to real earthquakes and those resulting from noise, unlikely signals or artifacts.
 182 Finally, given the large study area and the heterogeneous station coverage, the stacked signal
 183 response varies over time, making the choice of a detection threshold non-trivial. To address
 184 this, we implement a dynamic threshold approach based on the cumulative distribution
 185 function of the daily CNR. Assuming that most low-amplitude beams do not correspond to
 186 real events, we define the threshold at the inflection point, or “knee”, of the distribution
 187 (Figure 3c). However, in cases where the knee is not well-defined, we are aware that the
 188 uncertainty in event detection could increase.

189 To maintain a conservative yet effective detection criterion, we set the threshold at the
 190 97th percentile of the beam power distribution. We also note that values between the 95th
 191 and 99th percentiles can effectively distinguish potential seismic signals while reducing the
 192 likelihood of false detections. This adaptive approach ensures that the detection threshold
 193 dynamically adjusts to the empirical characteristics of the dataset, optimizing the balance
 194 between sensitivity and reliability.

195 2.3 Initial events relocation

196 As previously mentioned, the initial backprojection is highly sensitive to the spatial
 197 resolution of the 3D grid and the velocity model. To improve location accuracy, we employ
 198 the NonLinLoc-SSST-Coherence algorithm (Lomax, 2001; Lomax et al., 2009; Lomax &
 199 Savvaidis, 2022), which refines event locations using probabilistic inversion methods while
 200 accounting for uncertainties.

201 NonLinLoc uses the *a priori* P - and S -wave picks identified by PhaseNet, to perform
 202 a grid search and sample the likelihood of hypocenter locations (Figure S3). We also ap-
 203 ply Source-Specific Station Term (SSST) corrections, which iteratively refine travel-time
 204 estimates by minimizing residuals between observed and predicted seismic phase arrivals
 205 (Figure S4). This approach accounts for spatial velocity variations, producing a smoother
 206 station-specific velocity model and allowing travel-time corrections to adapt to regional
 207 heterogeneities, resulting in more precise and well-clustered earthquake locations.

208 Finally, we apply a relative relocation method based on waveform coherence (Lomax
 209 & Savvaidis, 2022), conceptually similar to other techniques such as HypoDD (Waldhauser,

210 2001) or GrowClust (Trugman & Shearer, 2017), but without relying on differential travel
 211 times. High waveform coherence, quantified by the maximum cross-correlation, suggests that
 212 close events originate from nearby sources. We stack the location PDFs of highly correlated
 213 events and relocate them within their shared probability region. This approach enhances
 214 location accuracy, even in regions with sparse station coverage and limited datasets, such
 215 as in our case.

216 2.4 Template matching

217 Template matching is a technique to identify new earthquakes with a low signal-to-noise
 218 ratio from existing examples (or templates) (Anstey, 1964; Gibbons & Ringdal, 2006; Shelly
 219 et al., 2007; Frank & Shapiro, 2014; Skoumal et al., 2014; Beaucé et al., 2018; Cabrera et
 220 al., 2021; Beaucé et al., 2022; Minetto et al., 2022). This process quantifies the similarity
 221 between seismic waveforms, triggering a new detection when the correlation is sufficiently
 222 high (Figure S5). We define as templates a subset of earthquakes with location uncertainties
 223 below 10 km of hypocentral distance. To avoid redundancy, which could result in multiple
 224 detections of the same earthquake, we take the first event among highly correlated events
 225 (more than 0.5 correlation coefficient). Each template consists of a 10 s signal window, focus-
 226 ing on the *P*-wave phase in the vertical component and the *S*-wave phase in the horizontal
 227 components.

228 We finally cross-correlate the continuous data with the templates in search for high
 229 correlation values. New detections are identified when the cross-correlation coefficient ex-
 230 ceeds a time-dependent threshold, calculated as 8 times the Root Mean Square (RMS) of
 231 each 30 min segments. We then assign the template location to every subsequently detected
 232 event. To ensure the catalog contains only unique events, we apply a combination of geo-
 233 graphic, temporal, and similarity-based filters. Events that occur within 4 s and 10 km of
 234 each other were assessed for redundancy. We perform an iterative removal events with lower
 235 inter-template correlation coefficients (<0.10) or higher location uncertainties, prioritizing
 236 the retention of the most reliable detections.

237 2.5 Magnitude and *b*-value estimation

238 To complete our earthquake catalog, we compute the moment magnitude using gener-
 239 alized parameters (see Table S1, and Hanks & Kanamori, 1979)

$$M_w = \frac{2}{3}(\log_{10} M_0 - 9.1), \quad (2)$$

240 where M_0 is the seismic moment, derived from the stacking and fitting of the Brune model
 241 (Brune, 1970) to the *S*-wave displacement spectra recorded by the seismic network (Satriano,
 242 2021). The obtained M_0 values are then integrated into Equation 2 to compute M_w . Mo-
 243 ment magnitude is advantageous for representing earthquake size, as it does not suffer from
 244 saturation and remains reliable across a broad range of seismic events. However, estimating
 245 M_w for small earthquakes is challenging because their related ground motion is often masked
 246 by background noise. Accurate estimation of M_w for these minor events relies heavily on
 247 the sensitivity of instruments and the density of near-field stations.

248 Therefore, for smaller events or when data quality is insufficient, we estimate M_w from
 249 a calibration of M_L to homogenize our catalog (Deichmann, 2017). For this purpose, we
 250 estimate a local magnitude, M_L , by simulating a Wood-Anderson seismograph (Richter,
 251 1935)

$$M_L = \log_{10} A + \log_{10} \frac{\delta}{100} + 0.00301(\delta - 100) + 3. \quad (3)$$

252 We use the default parameters from California as a reference (Table S2), which are enough
 253 to provide a practical comparative baseline (Equation 3). In this equation, A represents
 254 the peak-to-peak amplitude of the *S* wave recorded by the simulated Wood-Anderson seis-

255 mometer and δ is the hypocentral distance to each station (Bakun & Joyner, 1984; Satriano,
256 2021).

257 We analyze the frequency and distribution of magnitudes across our study area, with
258 the widely applied linear logarithmic relationship (Gutenberg & Richter, 1944)

$$\log_{10} N(\geq M) = a - bM, \quad (4)$$

259 where $N(\geq M)$ represents the cumulative number of earthquakes with magnitudes greater
260 than or equal to M . The constant a estimates the seismic activity level in the region, while
261 b indicates the relative proportion of high- to low-magnitude earthquakes, typically near
262 1. These parameters also serve to determine the catalog's magnitude of completeness M_c
263 defined as the minimum magnitude at which the likelihood of detecting all earthquakes
264 approaches 1. However, this analysis may be biased in cases of periodically low availability
265 of stations or general incompleteness within the dataset.

266 To address the challenges in estimating the b -value, we applied the b -more-incomplete
267 method (Lippiello & Petrillo, 2023), which builds upon the b -positive method (van der Elst,
268 2021) but improves accuracy by artificially increasing the level of incompleteness in the
269 catalog before estimating b . While the b -positive method calculates b from positive mag-
270 nitude differences between successive earthquakes, the b -more-incomplete method enhances
271 robustness by filtering out smaller events that could introduce bias due to partial detection.
272 This artificial filtering helps mitigate the effects of short-term aftershock incompleteness
273 (STAI), ensuring that the estimated b -value is less affected by time-dependent variations
274 in detection thresholds and to minimize the effects of overlapping coda waves and sparse
275 network coverage in the catalogs, resulting in a more accurate b -value estimation.

276 3 Results

277 3.1 Earthquake catalog

278 We first present our machine learning-based catalog that covers 10 months of after-
279 shock activity, recording 374,058 earthquakes from March 12, 2010, to January 24, 2011.
280 At first, we detect 99,137 events with a minimum of five P -wave and five S -wave arrival
281 picks. Figure 4 presents the three stages of the relocation process in two rows: the top row
282 illustrates the entire study area, while the bottom row provides a close-up view of Pichilemu
283 (34°S - 35°S), where aftershock activity was very intense. Figure 4a-a' shows the first stage
284 with absolute locations where the seismicity distribution appears mostly scattered. How-
285 ever, we can still distinguish two main types of earthquakes: a shallow component, related
286 to a crustal component, and a deeper component, with most events located up to 50 km in
287 depth, related to the subduction slab. In Figure 4a, we also identify that many events in
288 the outer-rise zone (offshore, north of the rupture area) are located at depths even below
289 40 km.

290 In a second stage, we relocate the events adjusting the time residuals for each station,
291 as shown in Figures 4b-b'. We now observe that most of the seismicity in the outer-rise zone
292 has shifted to shallower depths, clustered seismic patches are more evident along the rupture
293 zone and we identify clear patches with no detections, specially in the south. Finally, a total
294 of 41,250 events (41.6% of the initial catalog) are successfully relocated relative to nearby
295 events, as presented in Figures 4c-c'. Here seismic patches become less diffuse and we can
296 better distinguish geotectonic structures (e.g., Pichilemu fault system, Figures 4c').

297 From the relocation process, we initially identify 31,444 well-located earthquakes (with
298 location uncertainties below 10 km) to serve as templates for template matching. To pre-
299 vent redundant detections caused by highly similar events, we perform a waveform cross-
300 correlation analysis, removing duplicates and retaining a set of 8,894 unique templates.
301 Applying template matching with these templates results in the detection of 275,959 new
302 earthquakes, increasing the number of events by a factor 30. To maintain consistency with

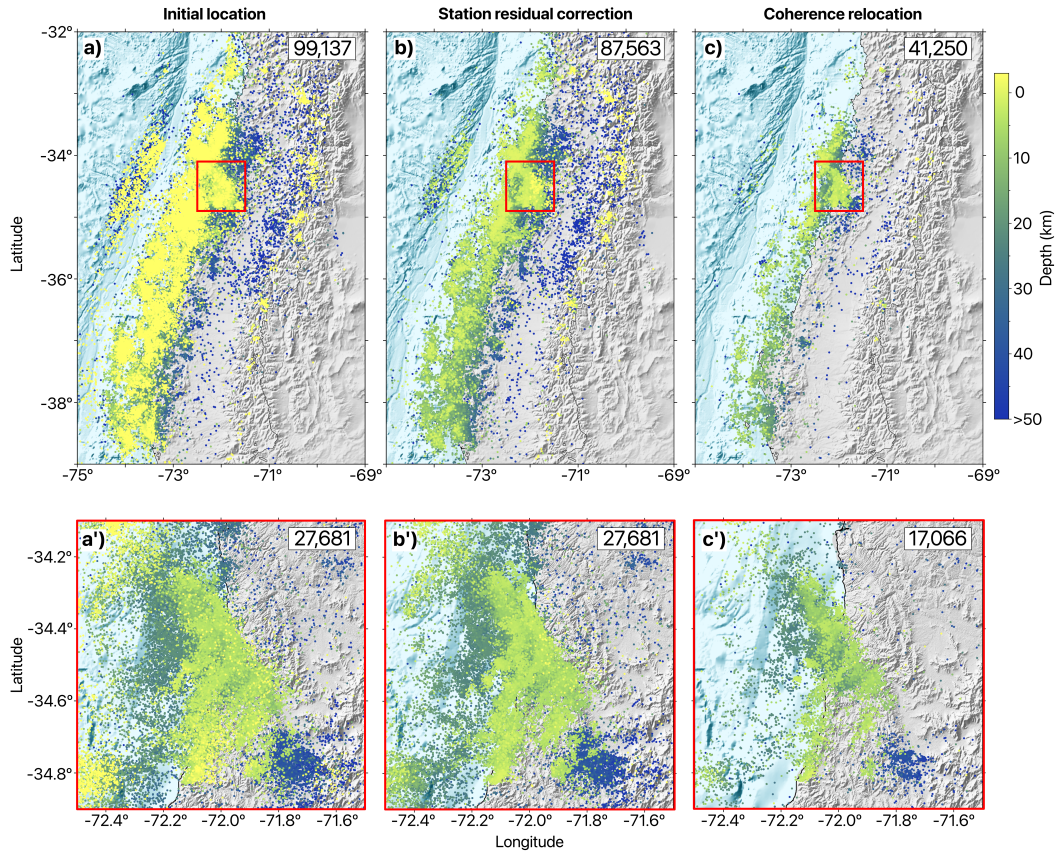


Figure 4. Earthquake locations at different steps of the relocation process. Panels (a–c) show the entire study area at different stages of relocation: (a) Initial locations based on automatic picks by PhaseNet. (b) Time residual corrections between observed picks and theoretical seismic phase arrivals, applied to the entire initial catalog. (c) Relative relocation based on coherence of nearby seismic signals, which could only be applied to a subset of earthquakes, primarily those near the IMAD network. (a'–c') Close-up view of the Pichilemu fault system, an area with a high concentration of aftershocks.

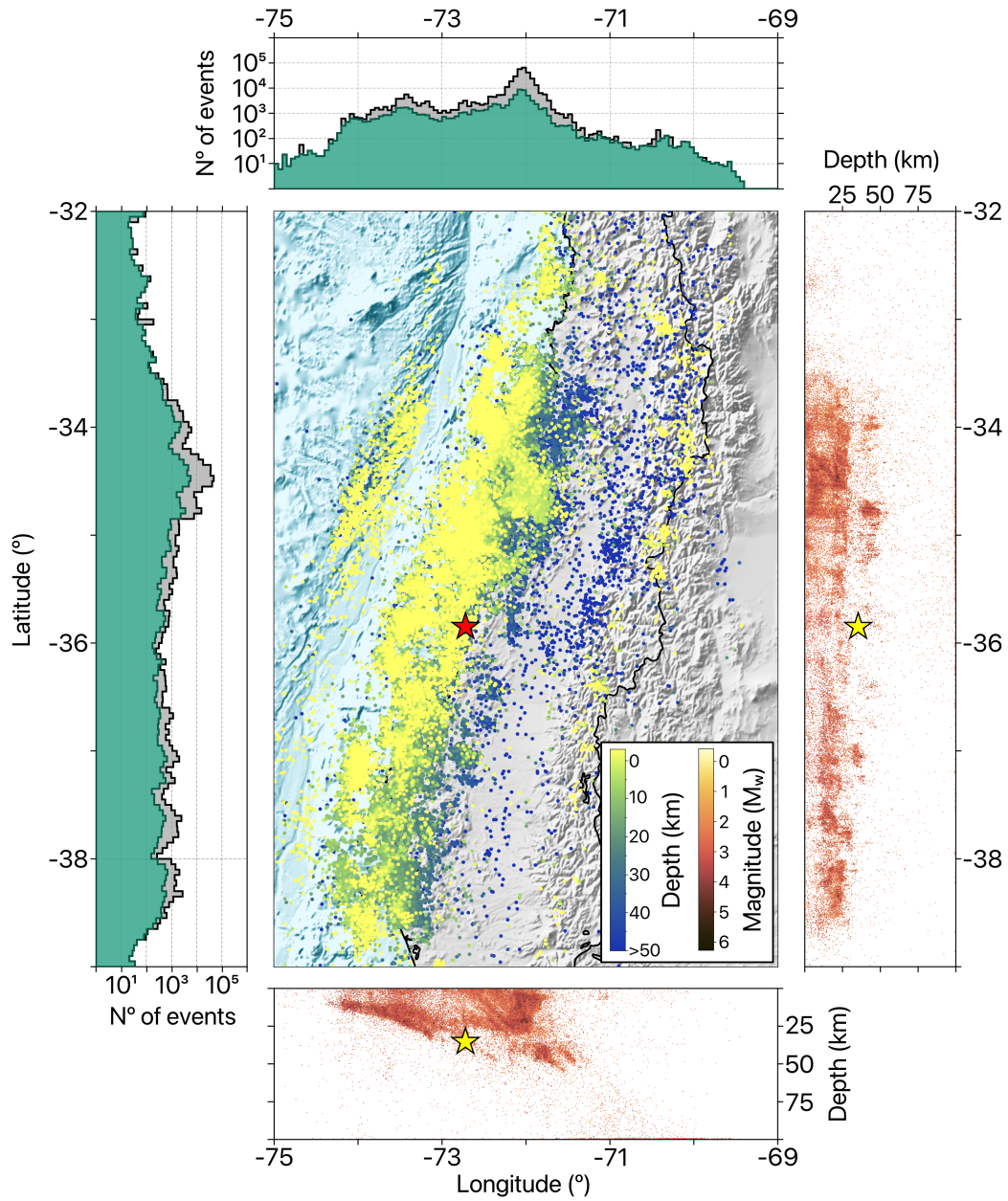


Figure 5. Spatial distribution of the aftershocks in the study area. The top and left panels respectively show the number of earthquakes as a function of longitude and latitude. The green histograms represent the initial catalog, while the grey histograms represent the final catalog after template matching. The right and bottom panels display stacked depth profiles of the earthquake catalog. The bottom panel clearly illustrates subduction across different longitudes, while the right panel shows the concentration of seismicity with latitude as a function of depth. The red star marks the location of the mainshock.

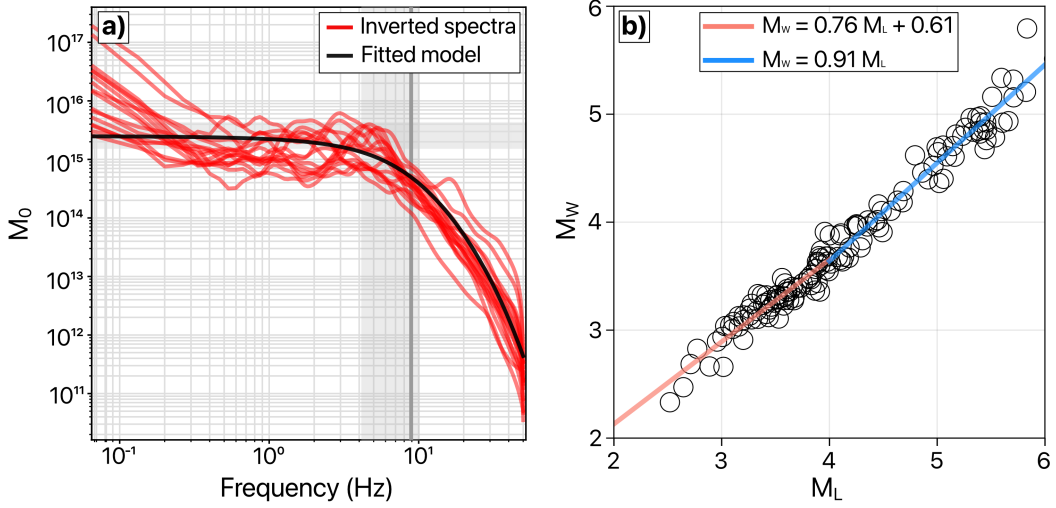


Figure 6. Magnitude estimation method for the earthquake catalog. (a) Seismic moment M_0 plotted against the frequency content of the seismic signal for an example event. Red lines show the displacement spectra recorded at different stations for this event, with Brune’s model fitted to the stacked spectra (black line). The vertical dark gray rectangle indicates the estimated corner frequency. (b) Local magnitude M_L calibration for moment magnitude M_w estimation for nearly 30,209 earthquakes in our catalog, represented by data with low standard deviation values.

303 the scope of this study, we assign the locations of these newly detected events to their cor-
 304 responding parent template, assuming a closely spaced source for each event. As shown in
 305 the histograms in Figure 5 (top and left panels), the green area represents the initial cata-
 306 log, while the gray area corresponds to the final catalog after template matching, with bin
 307 sizes of 0.1° . Most seismicity is concentrated in the Pichilemu area ($34\text{--}35^\circ\text{S}$, $71.5\text{--}72.5^\circ\text{W}$),
 308 where we identify the highest density of events both before and after template matching.

309 We estimate the local magnitude M_L for the entire catalog and the moment magnitude
 310 M_w for a subset of 145 reliable events. Figure 6a illustrates the stacking process of the
 311 displacement spectra from multiple stations for an earthquake, used to estimate the seismic
 312 moment M_0 . Based on this information, we calibrate M_L to estimate M_w for the entire
 313 dataset, such as

$$M_w = \begin{cases} 0.76M_L + 0.61 & \text{if } M_L \leq 4, \\ 0.91M_L & \text{otherwise.} \end{cases} \quad (5)$$

314 This approach homogenizes the catalog magnitude types, delivering M_w ranging from -0.34
 315 to 6.50 , with an average 1.86 and a completeness magnitude M_c of 1.7 . The majority of
 316 events cluster at lower magnitudes, with the first quartile at $M_w 1.49$, the median at M_w
 317 1.74 , and the third quartile at $M_w 2.12$. Approximately 90% of the events have magnitudes
 318 below $M_w 2.59$. Periodic spikes in event counts indicate intervals of increased seismicity,
 319 likely corresponding to aftershock sequences. Most events fall within the $M_w 2\text{--}3$ range,
 320 while larger magnitudes, up to $M_w 6$, are concentrated in the Pichilemu region, which also
 321 recorded the two largest aftershocks ($M_w 7$ and 6.9). However, the seismic network became
 322 fully operational only a few days after these two events, so they are not included in this
 323 catalog.

3.2 Frequency-magnitude distribution and b -value

The temporal variation in the number of available IMAD stations since March 12, 2010, is shown in Figure 7a, along with the location uncertainties of earthquakes. Station availability fluctuates significantly, specially after the first three months, where a steady decline is observed, aside from short week-long fluctuations. Toward the end of the period, station availability stabilizes at approximately 15 stations. These fluctuations directly affect earthquake detection and location accuracy, with periods of reduced station coverage corresponding to increased location uncertainties (Figure 7a). This effect is also evident in Figure 7b, where regions with a dense station coverage (Figure 1b), such as Pichilemu (34–35°S), exhibit a higher density of events. Conversely, regions with lower station availability exhibit detection gaps, particularly between 35 S and 37 S after 100 days from the start of the study. The larger-magnitude events are predominantly concentrated in the beginning of the sequence and mostly related to the Pichilemu area. As shown in Figure 7c, the magnitude distribution over time highlights a concentration of magnitudes around M_w 2. Looking at the earthquake detection rates (Figure 7c), we observe the expected decay over time, with occasional swarms that correspond to station reactivation. This emphasizes the large impact of station availability in the interpretation of earthquake catalogs.

We compute the b -value using two different methods, as illustrated in Figure 7d. For this analysis, we use batches of 6,000 earthquakes to estimate the b -value over time. The black line represents the b -values obtained using the classical maximum likelihood method for events above M_c , while the red line corresponds to estimates from the b -more-incomplete method (Lippiello & Petrillo, 2023). Notably, at the beginning of the sequence, b -values fluctuate between 1 and 1.3 until station availability begins to decline over time. As more stations become unavailable, we observe a progressive decrease in the b -value, reaching approximately 0.8.

4 Discussion

4.1 Geotectonic implications

This catalog provides a unprecedented high-quality view of the aftershock sequence of the 2010 Maule earthquake, particularly in the Pichilemu area, where the post-seismic activity was most intense (Figure 8, B-B'). The normal-faulting nature of this system and its potential reactivation within the area of highest coseismic slip have been documented (Fariás et al., 2011; Lange et al., 2012; Ryder et al., 2012; Lieser et al., 2014). Yet, we provide a more detailed analysis of the seismotectonic structure related to the Pichilemu fault system is illustrated in Figure 9, where we isolated the seismicity related to this fault system with HDBSCAN, a density-based clustering algorithm (Campello et al., 2013) often used a solution to distinguish earthquake patterns within catalogs (Essing & Poli, 2024). We observe a main fault is characterized by an azimuth-dip orientation of N40°W/S30°W and extends approximately 49 km (Figure 9, A-A'). Interestingly, the fault system exhibits distinct seismic patterns, with branches perpendicular to the main fault, forming an L-shaped distribution. This geometry suggests a complex conjugate fault system, which likely developed in response to crustal stress accommodation, similar to other documented cases of seismic sequences such as the M 6.5 Ludian earthquake (Li et al., 2024) and the M_w 7.1 Ridgecrest earthquake (Liu et al., 2019). The primary NW–SE striking fault dips at about 30°SW, while secondary NE–SW branches intersect it. Seismicity is concentrated between 5 and 20 km depth along these intersecting faults, reflecting a complex fault network consistent with stress redistribution following major earthquakes.

Offshore Pichilemu, we also observe an increased seismic activity in the outer-rise zone. This finding aligns with previous studies, which suggest that this seismicity is a direct response to the high co-seismic slip in the region, potentially resulting from the activation of shallow normal fault systems under extensional forces following large slip events (Moscoso

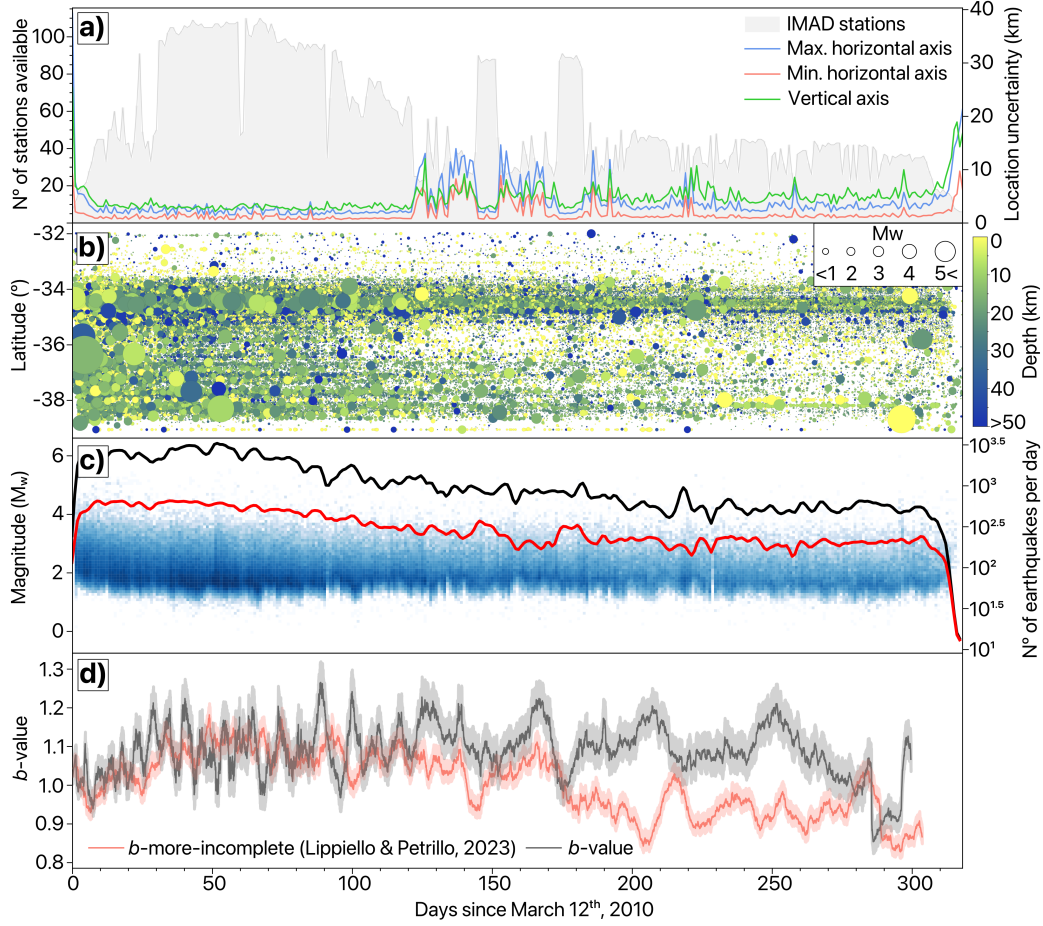


Figure 7. Temporal variations in (a) station availability (gray area) and earthquake location uncertainties (colored lines for maximum axis, minimum axis, and depth), (b) the spatial distribution in latitude, where circle size represents event magnitude and color indicates depth, (c) the magnitude variation in the final catalog (blue squares), and the trends accounting for the number of earthquake detected per day, from the initial catalog (red) and the final catalog (black), and (d) the estimated b -value using the b -more-incomplete method. Shaded areas indicate the uncertainty ranges for both methods.

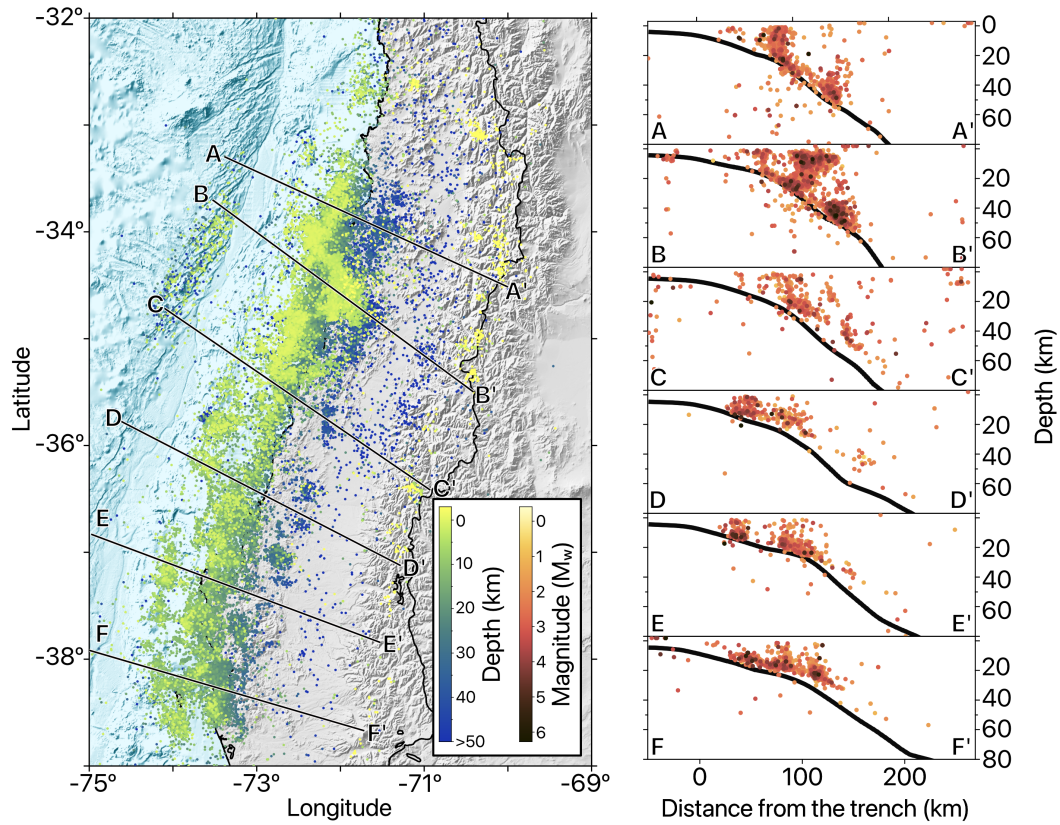


Figure 8. Spatial distribution of seismicity (colored dots) and profiles perpendicular to the subduction trench (black lines, A-F). On the left panel, color represents depth, while in the cross-sections on the right (A-F), color indicates magnitude. Black lines in the cross-sections correspond to the slab model (Slab 2.0, Hayes, 2018) for the subduction zone in this region.

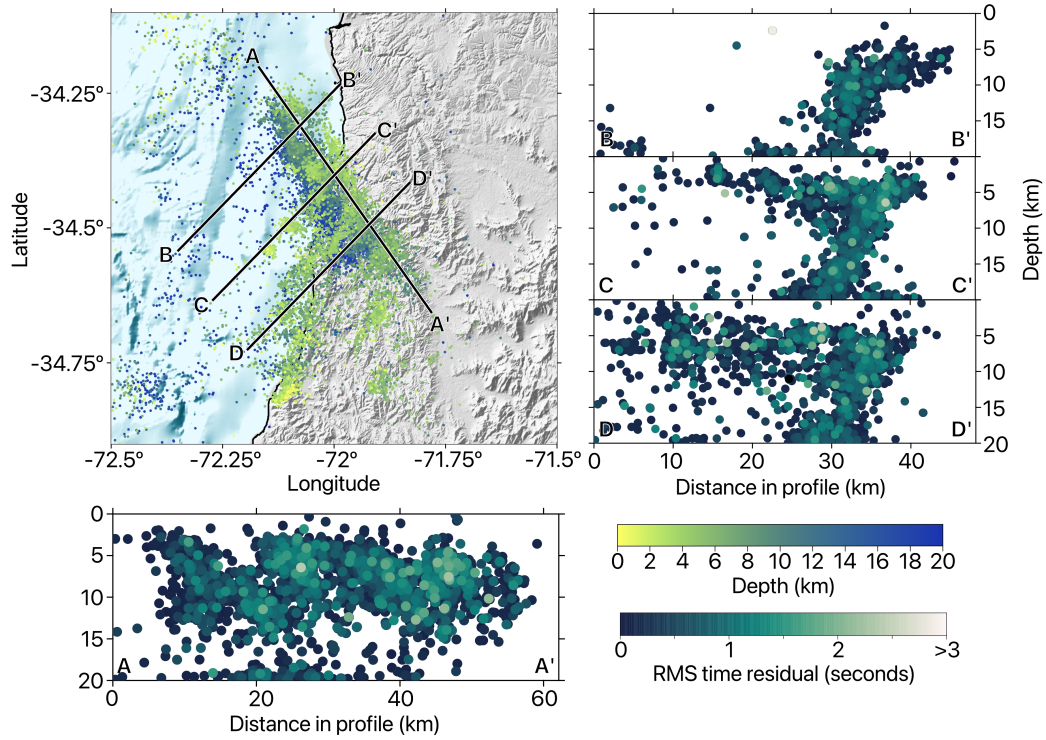


Figure 9. Spatiotemporal evolution of the Pichilemu fault system. Earthquakes are shown as dots color-coded by depth in the latitude-longitude map, and by the time residuals RMS in the cross-sections. Profiles along the black lines (A-D) include one in the main Pichilemu fault’s azimuthal direction (A-A’) and three perpendicular sections (B-D). The cross-sections illustrate the southwest dip direction of the northwest-trending fault and a series of conjugate faults, forming an L-shaped faulting system.

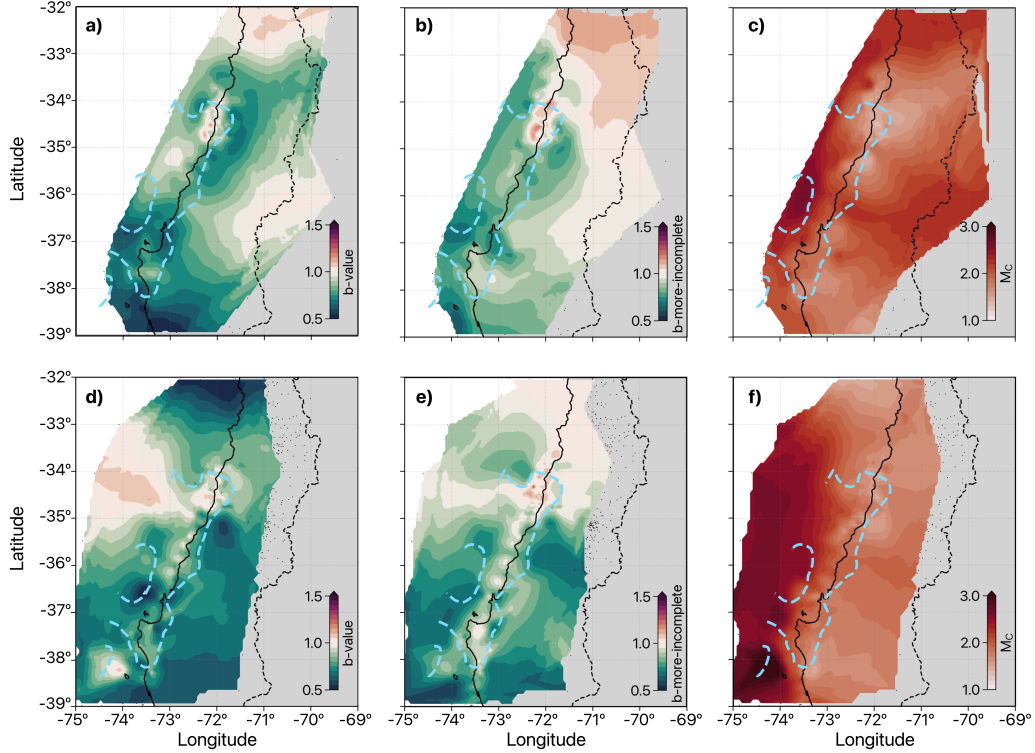


Figure 10. Spatial distribution of the b -value and M_c . We compute these values within earthquakes clusters of at least 100 earthquakes, for (a–c) shallower events associated with crustal seismicity, and (d–f) deeper slab-related and intraplate events. We estimate the classical b -value in (a) and (d), the b -more-incomplete in (b) and (e), and the M_c estimates in (c) and (f). The dashed blue line corresponds to the slip model (Yue et al., 2014) interpolated at 5 m.

374 & Contreras-Reyes, 2012; Lange et al., 2012; Rietbrock et al., 2012; J. A. Ruiz & Contreras-
 375 Reyes, 2015). However, earlier studies have located these events at depths exceeding 30 km,
 376 where brittle rupture is generally unexpected (Lange et al., 2012; Rietbrock et al., 2012). In
 377 contrast, our results improve the location accuracy of most of these events, showing a higher
 378 concentration at depths shallower than 20 km, as illustrated in Figure 8, sections B and C.
 379 Nonetheless, some depth-related artifacts persist, particularly for events below 40 km, where
 380 uncertainties remain high. These discrepancies may also stem from errors in phase-picking
 381 due to the considerable distance between the seismic sources and the network.

382 Intra-slab seismic activity associated with the subduction interface is present through-
 383 out the rupture zone. Notably, two distinct bands of seismicity are observed along the
 384 profiles: one at depths of 20 km to 35 km (Figure 8, A–F) and another, deeper band at
 385 approximately 50 km, primarily in Figure 8, A–C. Interestingly, a horizontal gap in seismic-
 386 ity is evident in the region closest to the mainshock (Figure 5), suggesting minimal post-
 387 mainshock activity in this area, likely due to significant coseismic stress release. While some
 388 seismicity does not align precisely with the slab model, it follows a consistent depth distribu-
 389 tion, highlighting distinct tectonic behaviors captured by this catalog. This underscores the
 390 need for further refinement of the slab contours by incorporating better-constrained event
 391 locations.

392 The temporal evolution of the b -value provides key insights into stress redistribution
 393 dynamics (Rivière et al., 2018). Here we compare two b -value estimation methods, the

394 traditional maximum likelihood (Aki, 1965) and the b -more-incomplete (Lippiello & Petrillo,
 395 2023) as illustrated in Figure 7d. During the first 170 days of the study period, both
 396 methods produce similar b -values, fluctuating between 0.9 and 1.3. However, few weeks
 397 after, the b -more-incomplete shows a gradual decrease, reaching values between 0.8-1.0,
 398 while the classical method remains relatively stable between 1.0 and 1.2. Because the b -
 399 more-incomplete method corrects for catalog incompleteness and compensates for station
 400 loss over time, this decreasing trend likely reflects a real change in seismic activity rather than
 401 an instrumental artifact. However, while template matching significantly improves small-
 402 earthquake detection, its application was not uniformly distributed throughout the study
 403 region, leading to heterogeneous detection rates. In regions with higher template density,
 404 b -values are likely more reliable, whereas lower template density regions remain low reliable.
 405 By day 280, both methods converge to values around 0.8, just before a M_w 6.2 earthquake.
 406 A decreasing b -value is commonly associated with increasing differential stress in the crust,
 407 potentially indicating conditions favorable for larger events (Scholz, 2015; Schorlemmer et
 408 al., 2005).

409 To analyze the spatial distribution of the b -value, we divide the catalog into two subsets:
 410 shallow seismicity associated with crustal activity occurring at least 10 km above the slab
 411 interface, and slab-related seismicity that includes events within the Nazca plate and intra-
 412 slab processes (Potin et al., 2024). To identify spatial patterns (Herrmann et al., 2022),
 413 we segment the catalog based on the longitude and latitude of events with a mini-batch
 414 k -means clustering strategy (Hartigan, 1975; Sculley, 2010), randomly selecting the number
 415 of clusters k between 200 and 1000. We disregard clusters with fewer than 200 events to
 416 ensure statistical robustness. We chose this approach for computational efficiency and ability
 417 to produce clusters with balanced variance. We estimate the magnitude of completeness
 418 withing each cluster, along with the classical b -value, and the b -more-incomplete, and assign
 419 it to every earthquake of a given cluster. To account for variability, this process is repeated
 420 over N iterations, averaging the b -values and M_c obtained for each earthquake at each
 421 iteration. Finally, we interpolate the results onto a regular grid using a randomly sampled
 422 subset of the catalog, averaging over multiple iterations to obtain a spatially smoothed
 423 representation of these parameters. This strategy proves to induce stable result over the set
 424 of parameters (number of iterations, size of the cluster, disregarded clusters) as shown by
 425 the convergence study in the supplementary materials.

426 Figure 10 presents the spatial distribution of the b -value, b -more-incomplete, and M_c
 427 for both crustal seismicity (Figure 10a-c) and slab-related seismicity (Figure 10d-f). The
 428 interpretation of the b -value requires caution, as it may be influenced by factors such as
 429 network coverage and noise levels. For instance, an increase in the b -value alongside a
 430 higher M_c likely indicates reduced detection capabilities, where only larger earthquakes are
 431 recorded (e.g., Geffers et al., 2022). The b -more-incomplete method mitigates this bias by
 432 removing lower-magnitude events occurring within 120 seconds of a preceding earthquake,
 433 unless the later event has a higher magnitude. Counterintuitively, enforcing an incomplete
 434 catalog in such cases leads to a more stable distribution, effectively reducing detection bias
 435 and improving the reliability of b -value estimates. Furthermore, these trends align with the
 436 temporal evolution shown in Figure 7d.

437 A pronounced discrepancy between both methods is particularly evident in the south-
 438 ern segment ($\sim 36^\circ\text{S}$ – 38°S), where Tassara et al. (2016) described a mechanically dry, highly
 439 coupled slab interface, where lower b -values are expected. The combination of lower b -
 440 more-incomplete values and high M_c suggests that classical b -value estimates are artificially
 441 inflated due to detection limitations rather than reflecting actual seismicity patterns. Con-
 442 versely, in the northern segment ($\sim 33^\circ\text{S}$ – 35°S), where fluid-rich subduction weakens the
 443 interface (Tassara et al., 2016; Arroyo-Solórzano & Linkimer, 2021), both methods consis-
 444 tently yield higher b -values, supporting the expected tectonic behavior. Additionally, regions
 445 with the highest co-seismic slip exhibit b -values consistently above 1 in both methods. In
 446 Figure 10, the blue dashed line represents the 5-meter slip contour from the coseismic slip

447 model (Yue et al., 2014). Notably, b -value reductions are concentrated around these zones,
 448 suggesting a potential correlation between high stress release (higher b -values) and stress
 449 accumulation (lower b -values) in adjacent areas. This pattern may provide further evidence
 450 of stress redistribution following major seismic events.

451 4.2 Comparison with previous catalogs

452 This aftershock sequence has already been the focus of previous studies, resulting in
 453 the development of earthquake catalogs. For instance, Lange et al. (2012) utilized auto-
 454 matic picking methods to compile a catalog of over 20,000 events spanning the first six
 455 months of the sequence. Similarly, Rietbrock et al. (2012) applied the STA/LTA triggering
 456 method with 2D velocity models, detecting and locating approximately 30,000 earthquakes.
 457 Additionally, Ryder et al. (2012) produced a catalog using comparable methods, although
 458 limited to a shorter period of two and a half months. These catalogs have served as the basis
 459 for numerous subsequent studies, including the characterization of afterslip seismic patterns
 460 (Agurto et al., 2012) and the development of velocity models through local earthquake to-
 461 mography, which have revealed new structural features in this segment of the subduction
 462 zone (Hicks et al., 2014). Major structures associated with the Maule earthquake rupture,
 463 such as those linked to the subduction slab and the crustal portion with high seismic ac-
 464 tivity near Pichilemu, are well-represented in these catalogs (e.g., Ryder et al., 2012) and
 465 are consistent in the seismicity distribution. However, the resolution of fine-scale seismic
 466 structures has remained limited.

467 Our study employs advanced detection and relocation techniques, particularly deep-
 468 learning-based seismic phase picking, to enhance the completeness and accuracy of the
 469 earthquake catalog. A key advantage is the improved resolution of fine-scale fault structures,
 470 enabled by detecting a significantly larger number of small-magnitude earthquakes. This
 471 improvement is primarily attributed to PhaseNet, which identified at least three times more
 472 seismic phases within the same dataset compared to conventional methods such as STA/LTA
 473 and SNR, as demonstrated in previous studies. The increased resolution provides deeper
 474 insights into the spatial distribution and connectivity of fault structures within the rupture
 475 zone, corroborating previous findings while uncovering additional structural details. For
 476 further details on relocation accuracy, refer to Text S1 and Figure S6. We successfully re-
 477 detect approximately 88 % of the events reported by Rietbrock et al. (2012) and 90 % of
 478 those cataloged by the Centro Nacional de Sismología de Chile (CSN) and the International
 479 Seismic Catalog (ISC) (Di Giacomo et al., 2018). The remaining events are likely excluded
 480 due to insufficient seismic picks in our dataset, limiting the processing of these signals. While
 481 these signals may correspond to real seismic events, they fail to meet the stringent criteria
 482 required for consistent processing within our methodology. By excluding them, we ensure
 483 the robustness, homogeneity, and reliability of our catalog.

484 Figure 11 compares the magnitude distribution, temporal evolution, and spatial cov-
 485 erage of seismicity in three catalogs: Rietbrock et al. (2012), the ISC catalog (Di Giacomo
 486 et al., 2018), and ours. While all catalogs achieve consistent detection completeness for
 487 $M_L \geq 3$, our catalog captures a significantly higher number of small-magnitude events
 488 ($M_L \leq 2$). This improvement is especially evident during periods of low station coverage,
 489 where our catalog maintains consistency, while detection capabilities decline in the other
 490 datasets. The seismicity rate, as shown in Figure 11d, highlights similar temporal trends
 491 across the three catalogs, with notable differences in the total number of events recorded.
 492 A significant observation is the local reduction in the detection capacity after larger earth-
 493 quakes, which leads to noticeable drops in the seismicity rate. This phenomenon reflects the
 494 saturation of seismic signals by the coda waves of larger events, which hinders the detection
 495 of smaller aftershocks. These biases, evident in all three catalogs, occur consistently at
 496 the same moments in the temporal distribution of seismicity. This highlights the impor-
 497 tance of accounting for detection limitations when interpreting seismic activity, as they can
 498 significantly affect the analysis of aftershock sequences and trends.

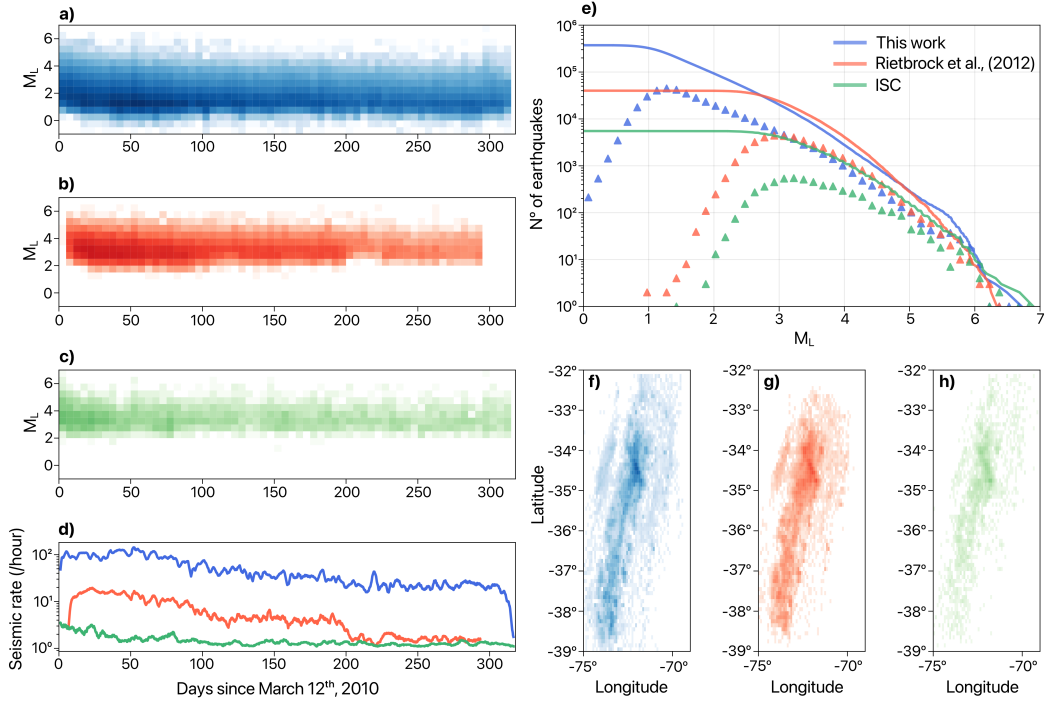


Figure 11. Comparison of earthquake catalogs based on magnitude distribution, temporal evolution, and spatial coverage. (a), (b), and (c): 2D histograms showing the distribution of local magnitudes (M_L) over time with bins of 5 days and 0.5 in magnitude. Blue represents the catalog presented in this study, red corresponds to the catalog by Rietbrock et al. (2012), and green denotes the catalog from the ISC. Lighter tones indicate lower data density, while darker tones represent higher densities. (d): Seismicity rate (events per hour) over time for the three catalogs, following the same color coding. (e): Magnitude-frequency distribution for the three catalogs. Solid lines represent the cumulative number of events following the Gutenberg-Richter law, while triangles indicate the number of earthquakes for each magnitude bin. (f), (g), and (h): Spatial distribution of seismicity in the rupture zone for each catalog.

499 The frequency-magnitude distribution of our catalog, compared to the catalogs of
 500 Rietbrock et al. (2012) and the ISC, is presented in Figure 11e. This comparison high-
 501 lights the improved detection capability of the proposed workflow, which achieves a lower
 502 magnitude of completeness by 1 to 2 orders of magnitude, significantly expanding the range
 503 of detectable seismic events. Panels Figure 11f–h show the overall shape of the seismic-
 504 ity distribution is consistent between catalogs, with a pronounced concentration around
 505 the Pichilemu region. However, our catalog reveals previously undetected zones of seismic
 506 activity, demonstrating the enhanced detection and location accuracy achieved with our
 507 workflow.

508 4.3 Workflow performance and limitations

509 In this study, we implement an automated detection-location workflow (Beaucé et al.,
 510 2024) and present a new catalog covering up to ten months of the Maule earthquake after-
 511 shock sequence. Our results demonstrate that, despite certain limitations in dataset quality,
 512 modern algorithms can significantly improve the completeness and precision of earthquake
 513 catalogs. However, the accuracy of these methods remains strongly dependent on the spa-
 514 tiotemporal coverage of the seismic network, underscoring the persistent challenges associ-
 515 ated with station density and distribution. For detection and location, we employed the
 516 automated seismic phase-picking model PhaseNet, a widely recognized tool for its effective-
 517 ness in phase detection (Tan et al., 2021; Chen et al., 2022; Feng et al., 2022; Jiang et al.,
 518 2022; Duan et al., 2023; Gong et al., 2023). This algorithm significantly enhanced detection
 519 capabilities while greatly reducing the time required for manual phase picking. In this study,
 520 we used the pre-trained *PhaseNet* model from northern California, which has demonstrated
 521 robust performance across diverse geotectonic contexts (Retailleau et al., 2022). However,
 522 its precision is still sensitive to high noise levels, particularly in regions with high anthro-
 523 pogenic sources, and its performance decreases for distant earthquakes where the *P-S* arrival
 524 time difference exceeds 30 s.

525 In addition, we used beamforming (Frank & Shapiro, 2014; Beaucé et al., 2019, 2022,
 526 2024) to obtain the source location likelihood of the initial catalog. However, this approach
 527 is highly sensitive to the chosen detection threshold in the daily composite network response
 528 (Figure 3). While previous studies have validated the use of fixed thresholds (e.g., Beaucé
 529 et al., 2024), our findings reveal the advantages of implementing a variable threshold for
 530 incomplete datasets. Specifically, we propose a criterion based on the 97th percentile of the
 531 daily cumulative density function, which dynamically adjusts to variations in data quality
 532 caused by fluctuations in station and channel availability. This threshold was optimized
 533 through performance testing to balance computational efficiency and detection accuracy,
 534 selecting the value that provided the best detection ratio. However, we acknowledge that
 535 this approach inherently imposes a detection rate, meaning that on days with low seismic
 536 activity, it may lead to an increased number of false detections. Despite this limitation,
 537 the adaptive thresholding method significantly improves the reliability of seismic records by
 538 reducing the likelihood of missed detections during periods of higher seismic activity.

539 The quality of seismic phase picking remains a critical factor in determining the ac-
 540 curacy of earthquake locations, with certain limitations persisting, particularly for distant
 541 events. Offshore events in the outer-rise zone, for example, present specific challenges due
 542 to the predominantly north-south orientation of the seismic array, which restricts azimuthal
 543 coverage and affects location precision. Nevertheless, the relocated hypocenters show a clear
 544 NNE alignment, consistent with the expected rupture geometry. Additionally, the accuracy
 545 of the velocity model plays a pivotal role in refining earthquake locations, emphasizing the
 546 need for further improvements in model precision. While a 1D velocity model is enough
 547 for many detection-location routines, it is inadequate for large regions like our study area,
 548 which is characterized by significant geological heterogeneities. In such cases, 3D tomogra-
 549 phy velocity models are highly beneficial as they capture velocity variations across latitude,
 550 longitude, and depth. However, while 3D models can provide valuable large-scale details,

551 their accuracy may still be limited in specific local contexts. For instance, in our case, a
552 1D model fails to adequately represent the velocity structure, yet even a 3D model (Potin
553 et al., 2024) can be oversimplified in certain zones, for example, in the outer-rise zone, the
554 velocity model remains poorly constrained due to limited seismic data. Similarly, in the
555 southern part of the rupture zone, the scarcity of seismic events hinders the accuracy of a
556 robust model. Therefore, an adapted approach was still required, as proposed for the scope
557 of this work introducing the slab geometry. Nonetheless, the results presented in Potin et
558 al. (2024) demonstrate notable outcomes at greater scales, and the velocity model employed
559 provides a valuable base for refining the Maule region’s tomography for future relocation
560 processes.

561 **5 Conclusion**

562 This study presents a catalog of the aftershock sequence of the 2010 M_w 8.8 Maule
563 earthquake in Chile from March 2010 to March 2011. We obtain the catalog from a re-
564 analysis of the past data with BPFM, an advanced detection-location workflow that relies
565 on PhaseNet-based phase picking, a high-precision relocation algorithms (NonLinLoc-SSST-
566 Coherence), and template matching to construct a high-resolution earthquake catalog. This
567 workflow enables the identification of over 375,000 earthquakes, which is 12 times more
568 than existing catalogs (Rietbrock et al., 2012). The catalog includes detailed uncertainties
569 in both location and magnitude, offering an unprecedented level of detail for understanding
570 post-seismic activity within the rupture zone.

571 One of the significant challenges addressed in this study is the varying availability
572 of the seismic network over time, and the overall temporal coverage of the experiment.
573 The IMAD mobile seismic network, deployed weeks after the mainshock, provided sparse
574 data, generating obstacles for accurate and consistent detection and location of seismic
575 events. By optimizing detection capabilities, we overcome these limitations to deliver a
576 precise and comprehensive catalog. This approach also helps to refine and uncover fine-
577 scale seismic structures with greater detail, consolidating patterns that were previously
578 scattered, particularly in regions of heightened activity, such as the northern rupture area
579 near Pichilemu. Additionally, this catalog spans a wide range of magnitudes (M_w -0.34
580 to 6.50), encompassing seismic events distributed across the subduction slab and shallow
581 crustal regions. It achieves a magnitude of completeness of about M_w 1.7, reducing it by an
582 order of magnitude compared to previous catalogs.

583 This study highlights the broader potential of automated workflows to advance earth-
584 quake monitoring and analysis. The methodology’s precision and adaptability ensure its
585 applicability to other earthquake sequences and diverse geotectonic contexts. Future re-
586 search can build on this work by integrating advanced velocity models to improve relocation
587 accuracy and by incorporating additional tomography. These developments could refine our
588 understanding of the physical mechanisms driving seismicity and provide critical insights
589 into subduction zone dynamics, the interplay between rupture dynamics, stress redistribu-
590 tion, and post-seismic deformation processes. Moreover, the results have practical implica-
591 tions for seismic hazard evaluation, offering tools to address challenges in mitigating risks
592 associated with large subduction earthquakes.

593 **Data Availability Statement**

594 The seismic data used in this study is publicly available through the RESIF ([https://](https://seismology.resif.fr)
595 seismology.resif.fr), IRIS (<https://www.iris.edu/hq/>), and GEOFON ([https://geofon](https://geofon.gfz.de/)
596 [.gfz.de/](https://geofon.gfz.de/)) data servers. It was collected as part of the temporary mobile network deployed
597 during the 2010 Maule aftershock sequence, with seismic instruments provided by CNRS-
598 INSU, IRIS/PASSCAL, GIPP (GFZ), and GEF/SeisUK. Supplementary materials, includ-
599 ing workflow details, are provided in Supplementary Figure S1, while the complete earth-
600 quake catalog is available in Supplementary File S2. The algorithms used in this study are

601 also open and accessible: the BackProjection and Matched Filter (BPMF) workflow can be
 602 found at https://github.com/ebeauce/Seismic_BPMF, the NonLinLoc-SSST-Coherence
 603 algorithm at <http://alomax.free.fr/nlloc/>, and SourceSpec at [https://github.com/](https://github.com/SeismicSource/sourcespec)
 604 [SeismicSource/sourcespec](https://github.com/SeismicSource/sourcespec). Additionally, the implementation of various b-value estima-
 605 tion methods is available at <https://github.com/caccioppoli/b-more-positive>.

606 Acknowledgments

607 This work was funded through the ANR-22-CPJ1-0020-01 program. E. Beaucé was funded
 608 by the Brinson Foundation. L.F. Bonilla was funded by project ANR E-City, AAPG 2021 –
 609 CES 22. Continuous seismic data was provided thanks to the collaborative efforts of IRIS,
 610 IPGP, ENS, and GFZ. Numerical computations were conducted on the S-CAPAD/DANTE
 611 platform at IPGP, France. We sincerely thank Sergio Ruiz and Raúl Madariaga for their
 612 valuable discussions on seismicity in the Maule region. We also acknowledge Javier Ojeda,
 613 Leoncio Cabrera, and Martin Vallée for their insightful contributions to discussions on seis-
 614 mic parameters relevant to this study. Additionally, we extend our appreciation to Antony
 615 Lomax, Jannes Münchmeyer, and Bertrand Potin for their constructive feedback on the
 616 event relocation process. We also thank the Andes-FrenSZ collaboration research program
 617 and associated researchers for their valuable comments and contributions. Finally, we are
 618 grateful to all researchers at IPGP, Universidad de Chile, and ISTerre who provided thought-
 619 ful insights, discussions, and feedback that contributed to improving this study.

620 References

- 621 Agurto, H., Rietbrock, A., Ryder, I., & Miller, M. (2012). Seismic-afterslip characteriza-
 622 tion of the 2010 mw 8.8 maule, chile, earthquake based on moment tensor inversion.
 623 *Geophysical Research Letters*, *39*(20).
- 624 Aki, K. (1965). Maximum likelihood estimate of b in the formula $\log n = a - bm$ and its
 625 confidence limits. *Bull. Earthquake Res. Inst., Tokyo Univ.*, *43*, 237–239.
- 626 Allen, R. (1982). Automatic phase pickers: Their present use and future prospects. *Bulletin*
 627 *of the Seismological Society of America*, *72*(6B), S225–S242.
- 628 Anstey, N. A. (1964). Correlation techniques—a review. *Geophysical Prospecting*, *12*(4),
 629 355–382.
- 630 Arroyo-Solórzano, M., & Linkimer, L. (2021). Spatial variability of the b-value and seismic
 631 potential in costa rica. *Tectonophysics*, *814*, 228951.
- 632 Bakun, W. H., & Joyner, W. B. (1984). The ml scale in central california. *Bulletin of the*
 633 *Seismological Society of America*, *74*(5), 1827–1843.
- 634 Båth, M. (1965). Lateral inhomogeneities of the upper mantle. *Tectonophysics*, *2*(6),
 635 483–514.
- 636 Beaucé, E., Frank, W. B., Paul, A., Campillo, M., & van Der Hilst, R. D. (2019). Systematic
 637 detection of clustered seismicity beneath the southwestern alps. *Journal of Geophysical*
 638 *Research: Solid Earth*, *124*(11), 11531–11548.
- 639 Beaucé, E., Frank, W. B., & Romanenko, A. (2018). Fast matched filter (fmf): An effi-
 640 cient seismic matched-filter search for both cpu and gpu architectures. *Seismological*
 641 *Research Letters*, *89*(1), 165–172.
- 642 Beaucé, E., Frank, W. B., Seydoux, L., Poli, P., Groebner, N., van der Hilst, R. D., &
 643 Campillo, M. (2024). Bpmf: A backprojection and matched-filtering workflow for
 644 automated earthquake detection and location. *Seismological Research Letters*, *95*(2A),
 645 1030–1042.
- 646 Beaucé, E., van der Hilst, R. D., & Campillo, M. (2022). Microseismic constraints on the
 647 mechanical state of the north anatolian fault zone 13 years after the 1999 m7. 4 izmit
 648 earthquake. *Journal of Geophysical Research: Solid Earth*, *127*(9), e2022JB024416.
- 649 Beck, S., Rietbrock, A., Tilmann, F., Barrientos, S., Meltzer, A., Oncken, O., ... Russo,
 650 R. M. (2014). Advancing subduction zone science after a big quake. *Eos, Transactions*
 651 *American Geophysical Union*, *95*(23), 193–194.

- 652 Bilek, S. L., & Lay, T. (2018). Subduction zone megathrust earthquakes. *Geosphere*, *14*(4),
653 1468–1500.
- 654 Brune, J. N. (1970). Tectonic stress and the spectra of seismic shear waves from earthquakes.
655 *Journal of geophysical research*, *75*(26), 4997–5009.
- 656 Cabrera, L., Ruiz, S., Poli, P., Contreras-Reyes, E., Osses, A., & Mancini, R. (2021). North-
657 ern chile intermediate-depth earthquakes controlled by plate hydration. *Geophysical*
658 *Journal International*, *226*(1), 78–90.
- 659 Campello, R. J., Moulavi, D., & Sander, J. (2013). Density-based clustering based on
660 hierarchical density estimates. In *Pacific-asia conference on knowledge discovery and*
661 *data mining* (pp. 160–172).
- 662 Campos, J., Hatzfeld, D., Madariaga, R., López, G., Kausel, E., Zollo, A., . . . Lyon-Caen,
663 H. (2002). A seismological study of the 1835 seismic gap in south-central chile. *Physics*
664 *of the Earth and Planetary Interiors*, *132*(1-3), 177–195.
- 665 Chen, H., Yang, H., Zhu, G., Xu, M., Lin, J., & You, Q. (2022). Deep outer-rise faults
666 in the southern mariana subduction zone indicated by a machine-learning-based high-
667 resolution earthquake catalog. *Geophysical Research Letters*, *49*(12), e2022GL097779.
- 668 Deichmann, N. (2017). Theoretical basis for the observed break in ml/m w scaling between
669 small and large earthquakes. *Bulletin of the Seismological Society of America*, *107*(2),
670 505–520.
- 671 Delouis, B., Nocquet, J.-M., & Vallée, M. (2010). Slip distribution of the february 27, 2010
672 mw= 8.8 maule earthquake, central chile, from static and high-rate gps, insar, and
673 broadband teleseismic data. *Geophysical Research Letters*, *37*(17).
- 674 Di Giacomo, D., Engdahl, E. R., & Storchak, D. A. (2018). The isc-gem earthquake
675 catalogue (1904–2014): status after the extension project. *Earth System Science Data*,
676 *10*(4), 1877–1899.
- 677 Duan, L., Zhao, C., Du, X., & Zhou, L. (2023). Machine learning-based automatic con-
678 struction of earthquake catalog for reservoir areas in multiple river basins of guizhou
679 province, china. *Earthquake Science*, *36*(2), 132–146.
- 680 Essing, D., & Poli, P. (2024). Unraveling earthquake clusters composing the 2014 alto tibe-
681 rina earthquake swarm via unsupervised learning. *Journal of Geophysical Research:*
682 *Solid Earth*, *129*(1), e2022JB026237.
- 683 Farías, M., Comte, D., Roecker, S., Carrizo, D., & Pardo, M. (2011). Crustal extensional
684 faulting triggered by the 2010 chilean earthquake: The pichilemu seismic sequence.
685 *Tectonics*, *30*(6).
- 686 Felzer, K. R., Abercrombie, R. E., & Ekstrom, G. (2004). A common origin for aftershocks,
687 foreshocks, and multiplets. *Bulletin of the Seismological Society of America*, *94*(1),
688 88–98.
- 689 Feng, T., Zhang, M., Xu, L., Wu, J., & Fang, L. (2022). Machine learning-based earthquake
690 catalog and tomography characterize the middle-northern section of the xiaojiang fault
691 zone. *Seismological Society of America*, *93*(5), 2484–2497.
- 692 Frank, W., & Shapiro, N. (2014). Automatic detection of low-frequency earthquakes (lfes)
693 based on a beamformed network response. *Geophysical Journal International*, *197*(2),
694 1215–1223.
- 695 Geffers, G., Main, I., & Naylor, M. (2022). Biases in estimating b-values from small earth-
696 quake catalogues: how high are high b-values? *Geophysical Journal International*,
697 *229*(3), 1840–1855.
- 698 Gibbons, S. J., & Ringdal, F. (2006). The detection of low magnitude seismic events
699 using array-based waveform correlation. *Geophysical Journal International*, *165*(1),
700 149–166.
- 701 Gong, J., Fan, W., & Parnell-Turner, R. (2023). Machine learning-based new earth-
702 quake catalog illuminates on-fault and off-fault seismicity patterns at the discov-
703 ery transform fault, east pacific rise. *Geochemistry, Geophysics, Geosystems*, *24*(9),
704 e2023GC011043.
- 705 Gutenberg, B., & Richter, C. F. (1944). Frequency of earthquakes in california. *Bulletin of*
706 *the Seismological society of America*, *34*(4), 185–188.

- 707 Hanks, T. C., & Kanamori, H. (1979). A moment magnitude scale. *Journal of Geophysical*
708 *Research: Solid Earth*, *84*(B5), 2348–2350.
- 709 Hartigan, J. A. (1975). *Clustering algorithms*. John Wiley & Sons, Inc.
- 710 Hayes, G. (2018). *Slab2-a comprehensive subduction zone geometry model: Us geological*
711 *survey data release*, doi: 10.5066. F7PV6JNV.
- 712 Herrmann, M., Piegari, E., & Marzocchi, W. (2022). Revealing the spatiotemporal complex-
713 ity of the magnitude distribution and b-value during an earthquake sequence. *Nature*
714 *Communications*, *13*(1), 5087.
- 715 Hicks, S. P., Rietbrock, A., Ryder, I. M., Lee, C.-S., & Miller, M. (2014). Anatomy of
716 a megathrust: The 2010 m8.8 maule, chile earthquake rupture zone imaged using
717 seismic tomography. *Earth and Planetary Science Letters*, *405*, 142–155.
- 718 Jiang, C., Zhang, P., White, M. C., Pickle, R., & Miller, M. S. (2022). A detailed earthquake
719 catalog for banda arc–australian plate collision zone using machine-learning phase
720 picker and an automated workflow. *The Seismic Record*, *2*(1), 1–10.
- 721 Lange, D., Tilmann, F., Barrientos, S. E., Contreras-Reyes, E., Methe, P., Moreno, M., . . .
722 et al. (2012). Aftershock seismicity of the 27 february 2010 mw 8.8 maule earthquake
723 rupture zone. *Earth and Planetary Science Letters*, *317*, 413–425.
- 724 Li, J., Hao, M., & Cui, Z. (2024). A high-resolution aftershock catalog for the 2014 m s
725 6.5 ludian (china) earthquake using deep learning methods. *Applied Sciences*, *14*(5),
726 1997.
- 727 Lieser, K., Grevemeyer, I., Lange, D., Flueh, E., Tilmann, F., & Contreras-Reyes, E. (2014).
728 Splay fault activity revealed by aftershocks of the 2010 mw 8.8 maule earthquake,
729 central chile. *Geology*, *42*(9), 823–826.
- 730 Lippiello, E., & Petrillo, G. (2023). b-more-incomplete and b-more positive: Insights on a
731 robust estimator of magnitude distribution. *arXiv preprint arXiv:2306.09574*.
- 732 Liu, C., Lay, T., Brodsky, E. E., Dascher-Cousineau, K., & Xiong, X. (2019). Coseismic
733 rupture process of the large 2019 ridgecrest earthquakes from joint inversion of geodetic
734 and seismological observations. *Geophysical Research Letters*, *46*(21), 11820–11829.
- 735 Lomax, A. (2001). *Nonlinloc home page*.
- 736 Lomax, A., Michelini, A., Curtis, A., & Meyers, R. (2009). Earthquake location, direct,
737 global-search methods. *Encyclopedia of complexity and systems science*, *5*, 2449–2473.
- 738 Lomax, A., & Savvaidis, A. (2022). High-precision earthquake location using source-specific
739 station terms and inter-event waveform similarity. *Journal of Geophysical Research:*
740 *Solid Earth*, *127*(1), e2021JB023190.
- 741 Madariaga, R., Métois, M., Vigny, C., & Campos, J. (2010). Central chile finally breaks.
742 *Science*, *328*(5975), 181–182.
- 743 Mancini, S., Segou, M., Werner, M. J., Parsons, T., Beroza, G., & Chiaraluce, L. (2022). On
744 the use of high-resolution and deep-learning seismic catalogs for short-term earthquake
745 forecasts: Potential benefits and current limitations. *Journal of Geophysical Research:*
746 *Solid Earth*, *127*(11), e2022JB025202.
- 747 Minetto, R., Helmstetter, A., Schwartz, S., Langlais, M., Nomade, J., & Guéguen, P. (2022).
748 Analysis of the spatiotemporal evolution of the maurienne swarm (french alps) based
749 on earthquake clustering. *Earth and Space Science*, *9*(7), e2021EA002097.
- 750 Moreno, M., Rosenau, M., & Oncken, O. (2010). 2010 maule earthquake slip correlates with
751 pre-seismic locking of andean subduction zone. *Nature*, *467*(7312), 198–202.
- 752 Moscoso, E. I., & Contreras-Reyes, E. (2012). Outer rise seismicity related to the maule,
753 chile 2010 mega-thrust earthquake and hydration of the incoming oceanic lithosphere.
754 *Andean Geology*, *39*(3), 564–572.
- 755 Mousavi, S. M., & Beroza, G. C. (2023). Machine learning in earthquake seismology. *Annual*
756 *Review of Earth and Planetary Sciences*, *51*(1), 105–129.
- 757 Ojeda, J., Ruiz, S., del Campo, F., & Carvajal, M. (2020). The 21 may 1960 mw 8.1
758 concepción earthquake: A deep megathrust foreshock that started the 1960 central-
759 south chilean seismic sequence. *Seismological Research Letters*, *91*(3), 1617–1627.
- 760 Peng, Z., & Zhao, P. (2009). Migration of early aftershocks following the 2004 parkfield
761 earthquake. *Nature Geoscience*, *2*(12), 877–881.

- 762 Potin, B., Ruiz, S., Aden-Antoniow, F., Madariaga, R., & Barrientos, S. (2024). A revised
763 chilean seismic catalog from 1982 to mid-2020. *Seismological Research Letters*.
- 764 Retailleau, L., Saurel, J.-M., Laporte, M., Lavayssière, A., Ferrazzini, V., Zhu, W., . . . et al.
765 (2022). Automatic detection for a comprehensive view of mayotte seismicity. *Comptes*
766 *Rendus. Géoscience*, *354*(S2), 153–170.
- 767 Richter, C. F. (1935). An instrumental earthquake magnitude scale. *Bulletin of the seis-*
768 *mological society of America*, *25*(1), 1–32.
- 769 Rietbrock, A., Ryder, I., Hayes, G., Haberland, C., Comte, D., Roecker, S., & Lyon-Caen,
770 H. (2012). Aftershock seismicity of the 2010 maule mw= 8.8, chile, earthquake:
771 Correlation between co-seismic slip models and aftershock distribution? *Geophysical*
772 *Research Letters*, *39*(8).
- 773 Rivière, J., Lv, Z., Johnson, P., & Marone, C. (2018). Evolution of b-value during the
774 seismic cycle: Insights from laboratory experiments on simulated faults. *Earth and*
775 *Planetary Science Letters*, *482*, 407–413.
- 776 Ross, Z. E., Idini, B., Jia, Z., Stephenson, O. L., Zhong, M., Wang, X., . . . et al. (2019). Hi-
777 erarchical interlocked orthogonal faulting in the 2019 ridgecrest earthquake sequence.
778 *Science*, *366*(6463), 346–351.
- 779 Ruiz, J. A., & Contreras-Reyes, E. (2015). Outer rise seismicity boosted by the maule 2010
780 mw 8.8 megathrust earthquake. *Tectonophysics*, *653*, 127–139.
- 781 Ruiz, J. A., Hayes, G. P., Carrizo, D., Kanamori, H., Socquet, A., & Comte, D. (2014).
782 Seismological analyses of the 2010 march 11, pichilemu, chile m w 7.0 and m w 6.9
783 coastal intraplate earthquakes. *Geophysical Journal International*, *197*(1), 414–434.
- 784 Ruiz, S., Aden-Antoniow, F., Baez, J. C., Otarola, C., Potin, B., del Campo, F., . . .
785 Bernard, P. (2017). Nucleation phase and dynamic inversion of the mw 6.9 val-
786 paraíso 2017 earthquake in central chile. *Geophysical Research Letters*, *44*(20),
787 10,290–10,297. Retrieved from [https://agupubs.onlinelibrary.wiley.com/doi/](https://agupubs.onlinelibrary.wiley.com/doi/abs/10.1002/2017GL075675)
788 [abs/10.1002/2017GL075675](https://doi.org/10.1002/2017GL075675) doi: <https://doi.org/10.1002/2017GL075675>
- 789 Ruiz, S., & Madariaga, R. (2018). Historical and recent large megathrust earthquakes in
790 chile. *Tectonophysics*, *733*, 37–56.
- 791 Ruiz, S., Madariaga, R., Astroza, M., Saragoni, G. R., Lancieri, M., Vigny, C., & Campos,
792 J. (2012). Short-period rupture process of the 2010 mw 8.8 maule earthquake in chile.
793 *Earthquake Spectra*, *28*(1-suppl), 1–18.
- 794 Ryder, I., Rietbrock, A., Kelson, K., Bürgmann, R., Floyd, M., Socquet, A., . . . Carrizo,
795 D. (2012). Large extensional aftershocks in the continental forearc triggered by the
796 2010 maule earthquake, chile. *Geophysical Journal International*, *188*(3), 879–890.
- 797 Salazar, K., & McNutt, M. (2011). Report on the 2010 chilean earthquake and tsunami
798 response. *Reston, Virginia: US Geological Survey*.
- 799 Satriano, C. (2021). Sourcespec–earthquake source parameters from s-wave displacement
800 spectra. *Zenodo*.
- 801 Scholz, C. H. (2015). On the stress dependence of the earthquake b value. *Geophysical*
802 *Research Letters*, *42*(5), 1399–1402.
- 803 Schorlemmer, D., Wiemer, S., & Wyss, M. (2005). Variations in earthquake-size distribution
804 across different stress regimes. *Nature*, *437*(7058), 539–542.
- 805 Sculley, D. (2010). Web-scale k-means clustering. In *Proceedings of the 19th international*
806 *conference on world wide web* (pp. 1177–1178).
- 807 Shelly, D. R., Beroza, G. C., & Ide, S. (2007). Non-volcanic tremor and low-frequency
808 earthquake swarms. *Nature*, *446*(7133), 305–307.
- 809 Skoumal, R. J., Brudzinski, M. R., Currie, B. S., & Levy, J. (2014). Optimizing multi-
810 station earthquake template matching through re-examination of the youngstown,
811 ohio, sequence. *Earth and Planetary Science Letters*, *405*, 274–280.
- 812 Steve Roecker, & Ray Russo. (2010). *Ramp response for 2010 chile earthquake*. International
813 Federation of Digital Seismograph Networks. Retrieved from [https://www.fdsn.org/](https://www.fdsn.org/networks/detail/XY_2010/)
814 [networks/detail/XY_2010/](https://www.fdsn.org/networks/detail/XY_2010/) doi: 10.7914/SN/XY_2010
- 815 Tan, Y. J., Waldhauser, F., Ellsworth, W. L., Zhang, M., Zhu, W., Michele, M., . . . Segou,
816 M. (2021). Machine-learning-based high-resolution earthquake catalog reveals how

- 817 complex fault structures were activated during the 2016–2017 central italy sequence.
 818 *The Seismic Record*, 1(1), 11–19.
- 819 Tassara, A., Soto, H., Bedford, J., Moreno, M., & Baez, J. C. (2016). Contrasting amount
 820 of fluids along the megathrust ruptured by the 2010 maule earthquake as revealed by
 821 a combined analysis of aftershocks and afterslip. *Tectonophysics*, 671, 95–109.
- 822 Trugman, D. T., & Shearer, P. M. (2017). Growclust: A hierarchical clustering algorithm
 823 for relative earthquake relocation, with application to the spanish springs and sheldon,
 824 nevada, earthquake sequences. *Seismological Research Letters*, 88(2A), 379–391.
- 825 van der Elst, N. J. (2021). B-positive: A robust estimator of aftershock magnitude dis-
 826 tribution in transiently incomplete catalogs. *Journal of Geophysical Research: Solid*
 827 *Earth*, 126(2), e2020JB021027.
- 828 Vigny, C., Socquet, A., Peyrat, S., Ruegg, J.-C., Métois, M., Madariaga, R., ... et al.
 829 (2011). The 2010 m w 8.8 maule megathrust earthquake of central chile, monitored
 830 by gps. *Science*, 332(6036), 1417–1421.
- 831 Vilotte, J., & et al. (2011). Seismic network xs: Chile maule aftershock temporary experi-
 832 ment (resif-sismob). *RESIF-Réseau Sismologique et géodésique Français*.
- 833 Waldhauser, F. (2001). hypodd—a program to compute double-difference hypocenter loca-
 834 tions (hypodd version 1.0-03/2001). *US Geol. Surv. Open File Rep.*, 01, 113.
- 835 White, M. C., Fang, H., Nakata, N., & Ben-Zion, Y. (2020). Pykonal: a python package
 836 for solving the eikonal equation in spherical and cartesian coordinates using the fast
 837 marching method. *Seismological Research Letters*, 91(4), 2378–2389.
- 838 Yao, D., Walter, J. I., Meng, X., Hobbs, T. E., Peng, Z., Newman, A. V., ... Protti,
 839 M. (2017). Detailed spatiotemporal evolution of microseismicity and repeating earth-
 840 quakes following the 2012 mw 7.6 nicoya earthquake. *Journal of Geophysical Research:*
 841 *Solid Earth*, 122(1), 524–542.
- 842 Yue, H., Lay, T., Rivera, L., An, C., Vigny, C., Tong, X., & Baez Soto, J. C. (2014).
 843 Localized fault slip to the trench in the 2010 maule, chile mw= 8.8 earthquake from
 844 joint inversion of high-rate gps, teleseismic body waves, insar, campaign gps, and
 845 tsunami observations. *Journal of Geophysical Research: Solid Earth*, 119(10), 7786–
 846 7804.
- 847 Zhu, W., & Beroza, G. C. (2019). Phasenet: a deep-neural-network-based seismic arrival-
 848 time picking method. *Geophysical Journal International*, 216(1), 261–273.